CHAPTER FOUR

The various solids prepared composing of Mo, V, Te, Nb and oxides of the support are further characterised to define their structural, thermal and chemical properties. This information would directly contribute to the understanding of catalyst synthesis and the defects properties of the catalyst, which in turn is crucial to a systematic and rational approach in catalyst design.

4.1 Surface Area Measurement

Nitrogen physisorption with the application of Brunauer-Emmett-Teller (BET) method was used to determine the specific surface areas of unpromoted and promoted Mo-V-Te-Nb-O_x catalyst systems.

4.1.1 Unpromoted $Mo_1V_{0.3}Te_{0.23}Nb_{0.12}O_x$ catalyst system

a) Effect of Pre-calcination Temperature

Table 4.1 show the total surface area of unpromoted $Mo_1V_{0.3}Te_{0.23}Nb_{0.12}O_x$ catalyst prepared by slurry method and subsequently pre-calcine at various temperatures to see the effect of pre-calcination. After that the catalyst was calcine at 873 K under argon for 2 hour. Previously the calcinations temperature of $Mo_1V_{0.3}Te_{0.23}Nb_{0.12}O_x$ catalysts system was evaluated in the temperatures of 873, 898, 923, 948, 973, 998, 1023 and 1048 K. Subsequently, the best calcinations temperature was found to be at 873 K. S_{BET} represents for specific surface areas ($cm^3\ gram^{-1}$).

Table 4.1: BET Result for $Mo_1V_{0.3}Te_{0.23}Nb_{0.12}O_x$ catalyst system at different pre-calcination temperatures.

Catalysts	Pre-Calcination Temperature (K)	S_{BET} ($m^2 g^{-1}$)
MoVTeNbOx (I)	448	2.3
MoVTeNbOx (II)	498	2.7
MoVTeNbOx (III)	548	10.5
MoVTeNbOx (IV)	598	5.4

The total surface area of unpromoted $Mo_1V_{0.3}Te_{0.23}Nb_{0.12}O_x$ increase gradually with increasing pre-calcination temperature, but when the precalcination temperature is higher than 548 K the total surface area immediately decreases. Andersson *et.al* stated that the specific surface areas of unpromoted Mo-V-Te-Nb-Ox catalyst could be in the range of 1.0 m^2g^{-1} to 11.0 m^2g^{-1} respectively [72]. From the results, we found that the different pre-calcination temperatures affect the surface area of the catalyst. This is because pre-calcination changes the morphology of the catalyst particle and at higher temperature the surface will become more porous until to a certain temperature (~548 K), then the total surface of catalysts decreases.

Temperature is an important factor for catalyst deactivation; at high temperature the catalyst starts to lose catalytic surface area due to crystal growth of the catalytic phase. These results are in agreement with the XRD diffractogram, which shows improvement in the crystalline phase when the temperature increases. From here we can conclude that the best precalcination temperature for this catalysts system is at ~548 K. This catalyst system gives isotherms Type III with the present of hysteresis loop, indicating the presence of mesopores and multiple layers condensation, and the hysteresis loop of type E, indicating the presence of pores having varying width [56].

b) Effect of Viscosity Enhancer

Table 4.2 shows the total surface area of unpromoted $Mo_1V_{0.3}Te_{0.23}Nb_{0.12}O_x$ catalyst systems with the addition of polyethylene glycol (PEG) or hydroxyl ethyl cellulose (HEC) as viscosity enhancer. The catalyst was pre-calcined at 548 K and subsequently calcined at 873 K under argon for 2 hour. S_{BET} represents specific surface areas (cm^3 $gram^{-1}$).

Table 4.2: BET result for $Mo_1V_{0.3}Te_{0.23}Nb_{0.12}O_x$ catalyst system with the addition of PEG or HEC as viscosity enhancer.

Catalysts	Viscosity Enhancer	S_{BET} (m^2g^{-1})
MoVTeNbOx (III)	SR	10.5
MoVTeNbOx + PEG	PEG	6.0
MoVTeNbOx + HEC	HEC	5.5

The main point of adding (PEG) or (HEC) during the preparation of the catalyst system is to ensure that no premature precipitation by any of the four metal components occurs prior to the drying step. Forcing precipitation of multi-components at a common point has the advantage of a more homogeneous precipitation necessary for uniform quality. This catalyst also gives isotherms of Type III with the present of hysteresis loop, indicating the presence of mesopores. The hysteresis loop is Type E, indicating the presence of pores having varying width.

The total surface areas of these catalysts are reduced by 50% compared to the standard reference catalyst. However, not much difference is observed to the surface area with the addition of different types of viscosity enhancer where the surface areas

for both systems are around 5.0 m^2g^{-1} to 6.0 m^2g^{-1}. The reduction in surface area of the two samples is not surprising, as the addition of bulky viscosity enhancers to the system would inevitably get deposited onto their external and internal surfaces. This is further supported by the reduction of the effective pore volume. Interestingly, the reduction of the pore volume has not changed the shape of the mesopores nor the pore size distribution seen in the adsorption isotherms in *Figure 4.1 and 4.2.* Part of the bulky viscosity enhancers, PEG, is inside the pores and they did not block the accessibility to the inside of the pore network. There is a subtle difference in the surface area between the PEG-added and HEC-added samples. In both cases, the viscosity enhancers are mostly on the outside of the MoVTe system and has effectively induced an agglomeration of both components, resulting in bigger particles giving rise to a reduction in surface area. The MoVTe system though has very little porosity of 0.1 m^2g^{-1} suffers a further loss when using HEC viscosity enhancers. It clearly shows that the HEC viscosity enhancers is too bulky to enter into the pore and gets deposited outside and has probably blocked the pore mouth MoVTe giving rise to a practically total loss of pore volume. Nevertheless, the HEC added MoVTe still has comparable surface, which can be attributed to very small particles.

c). Effect of Precursor

Tables 4.3 show the total surface area of unpromoted $Mo_1V_{0.3}Te_{0.23}Nb_{0.12}O_x$ catalyst system prepared via citric acid route to see the effect of precursor. The catalysts were pre-calcined at 548 K and calcined at 873 K under argon for 2 hour. S_{BET} represents the specific surface areas (cm^3gram^{-1}).

Table 4.3: BET result for $Mo_1V_{0.3}Te_{0.23}Nb_{0.12}O_x$ catalyst system prepared via citric acid route.

Catalysts	Citric acid (Ratio)	S_{BET} (m^2g^{-1})
MoVTeNbOx (III)	SR	10.5
MoVTeNbOx (1:1)	1:1	0.8
MoVTeNbOx (1:2)	1:2	0.8

The catalyst systems prepared from citric acid show a drastic reduction in surface area, practically nil as shown in Table 4.3. The surface area obtained is less than 1 m^2g^{-1}, a reduction by a factor of ten from the standard preparation method sample, SR. With such low surface area, the corresponding values obtained for pore volume are questionable. The adsorption isotherms obtained to deduce the pore volume are marginalized. The severe loss in surface area could be explained by various possible reasons:

- Leaching of the pre-formed MoVTe precipitates
- Exposing the MoVTe metal complexes ions in solutions in acidic environment via the addition of citric acid is unfavorable for their precipitation
- Sintering of MoVTe induced during the highly exothermic calcinations steps.

From this we can conclude that $Mo_1V_{0.3}Te_{0.23}Nb_{0.12}O_x$ prepared from ammonium precursor gives higher surface area compared with citric acid precursor. The advantage of using such bidentate should not be ruled out but careful calcinations regime could reveal the strength of complexing transition metal ions with citrate ion complexes.

4.1.2 Promoted $Mo_1V_{0.3}Te_{0.23}Nb_{0.12}MeO_x$ Catalysts System.

a) Effect of Promoter

Table 4.4 show the information obtained from the nitrogen physisorption on promoted $Mo_1V_{0.3}Te_{0.23}Nb_{0.12}MeO_x$ catalysts system with Ni-, Cr- and Co- as promoter prepared at two different weight loading (0.05 and 0.005). Previously the $Mo_1V_{0.3}Te_{0.23}Nb_{0.12}O_x$ catalysts system was screened after the addition of various transition metals such as Ni, Cr, Co, Mn, Fe, Ce, La, and Ph as a promoter. The Cr, Ni and Co metal promoter was shown to give a good catalytic performance compared to other metals. S_{BET} represents for specific surface areas ($cm^3\ gram^{-1}$).

Table 4.4: BET result for $Mo_1V_{0.3}Te_{0.23}Nb_{0.12}O_x$ catalyst system with the addition of various metals as a promoter (Ni-, Cr- and Co-) prepared at two different weight loading 0.05 and 0.005 atomic percent.

Catalysts	Promoter	S_{BET} ($m^2\ g^{-1}$)
MoVTeNbOx (III)	SR	10.5
MoVTeNb Ni Ox (I)	**Ni (0.05 at%)**	10.6
MoVTeNb Ni Ox (II)	Ni (0.005 at%)	7.3
MoVTeNbCr Ox (I)	**Cr (0.05 at%)**	11.5
MoVTeNbCr Ox (II)	Cr (0.005 at%)	9.4
MoVTeNbCoOx (I)	**Co (0.05 at%)**	5.3
MoVTeNbCoOx (II)	Co (0.005 at%)	10.6

This catalyst systems show adsorption isotherms of Type III with the presence of hysteresis loop, indicating the presence of mesopores and the hysteresis loop is of Type E, indicating the presence of pores having varying width.

The total surface area of these catalysts fluctuates in the range of 10 to 5 m^2g^{-1} whilst the pore volume shows negligible changes when the standard system were promoted with various promoters, Ni, Cr and Co. Surprisingly, the surface areas of Ni- and Cr-promoted catalysts increase when the weight loading of Ni- and Cr- promoter increases from 0.005 to 0.05. One would expect the low dosage of promoter added to MoVTe would not significantly perturb the initial surface area of the standard recipe catalysts whilst relatively higher dosage of 0.05 probably could modify the texture of the catalysts. It is taken that the variation of ± 3 m^2g^{-1} in surface area is within the experimental repeatability rather than inherent of the treatment that the systems have been subjected. Co- promoted MoVTe catalysts supports the deduction that at low loading of promoter the texture of the initial MoVTe would be unchanged. Increasing the loading of Co to the MoVTe system witnessed a 50% reduction in surface area. This effect is because of the abundance of cobalt electron in the periodic table compared with chromium.

From the BET surface area results we can anticipate that the higher surface area catalysts would exhibit higher activity. Hence, the surface area result is one of the major contributive factors governing catalyst activity. From the overall result also, the p/p_o range was found to be maintained at around 0.01 to 0.03. This is shown that the BET equation is linear and the BET plot can be expected give a true yield value. Sing *et al.* stated that BET equation requires a linear relation between 0.05 and 0.3 [56].

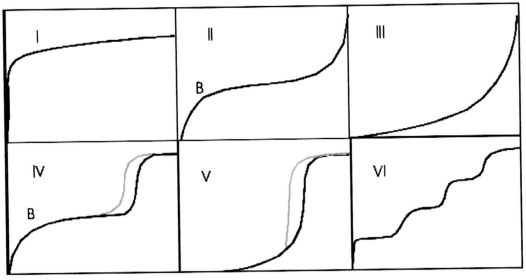

Figure 4.1: Six types of BET isotherm profiles according to IUPAC (Sing et.al) [56].

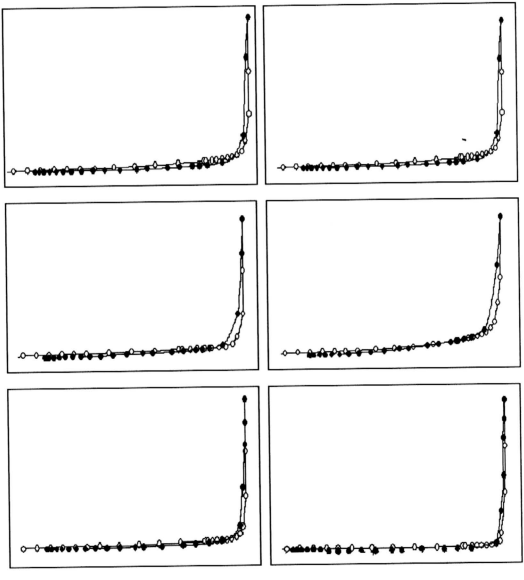

Figure 4.2: BET profiles for unpromoted and promoted Mo-V-Te-Nb-O_x catalysts.

4.2 Element Composition

4.2.1 Unpromoted Mo-V-Te-Nb-Ox catalyst system

a) Effect of Precalcine Temperature

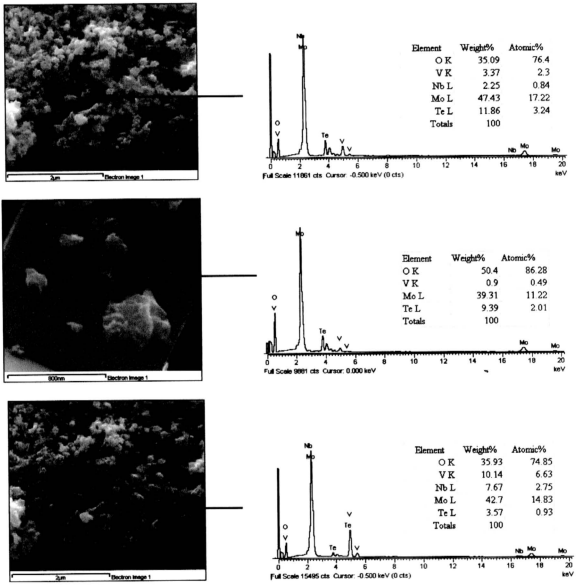

Element	Weight%	Atomic%	Melting point (^{O}C)
O K	35.51	75.63	-
V K	6.76	4.47	1915
Nb L	4.96	1.80	2468
Mo L	45.07	16.03	1620
Te L	**7.72**	**2.09**	450
Totals	**100.00**	**100.00**	

Figure 4.3: SEM-image (left) and EDX (right) of the final $Mo_1V_{0.3}Te_{0.23}Nb_{0.12}O_x$ catalyst pre-calcine at 448 K and calcine at 873 K under argon.

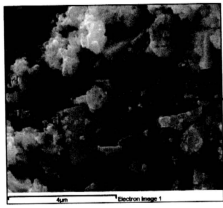

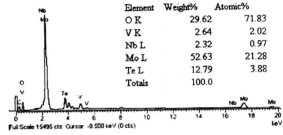

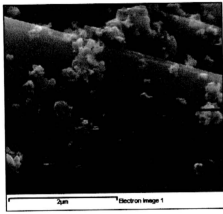

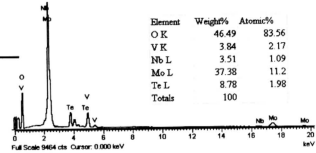

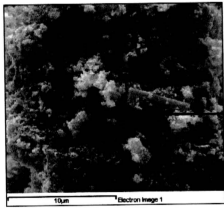

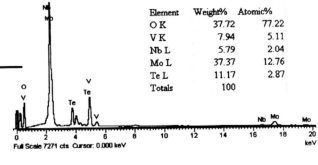

Element	Weight%	Atomic%	Melting point (^{O}C)
O K	37.75	77.54	-
V K	4.59	2.97	1915
Nb L	3.68	1.30	2468
Mo L	43.81	15.48	1620
Te L	**10.17**	**2.71**	450
Totals	**100.00**	**100.00**	

Figure 4.4: SEM-image (left) and EDX (right) of the final $Mo_1V_{0.3}Te_{0.23}Nb_{0.12}O_x$ catalyst pre-calcine at 498 K and calcine at 873 K under argon.

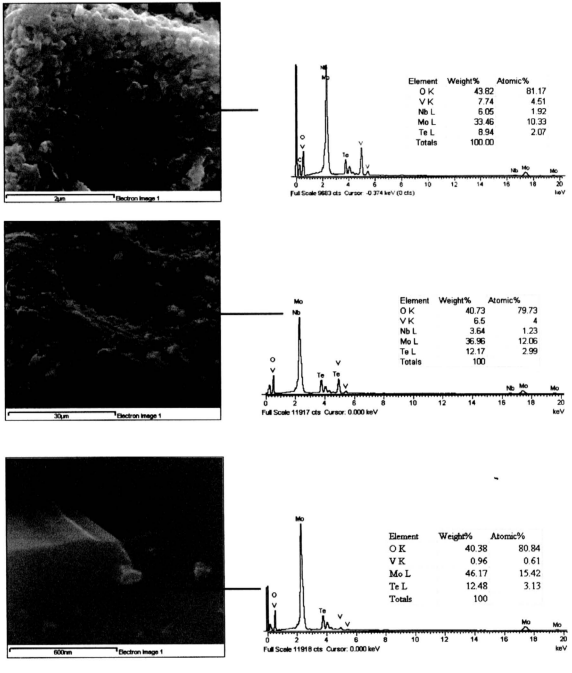

Element	Weight%	Atomic%	Melting point (^{O}C)
O K	40.86	79.41	-
V K	7.43	4.57	1915
Nb L	4.97	1.67	2468
Mo L	34.97	11.43	1620
Te L	**11.77**	**2.91**	450
Totals	**100.00**	**100.00**	

Figure 4.5: SEM-image (left) and EDX (right) of the final $Mo_1V_{0.3}Te_{0.23}Nb_{0.12}O_x$ catalyst pre-calcine at 548 K and calcine at 873 K under argon.

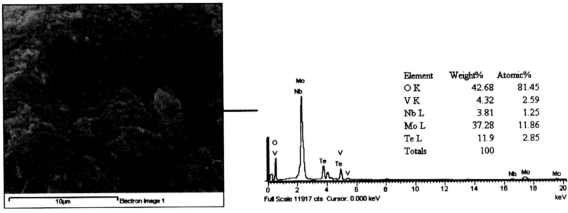

Element	Weight%	Atomic%	Melting point (^{O}C)
O K	39.14	78.79	-
V K	5.96	3.81	1915
Nb L	3.45	1.19	2468
Mo L	37.94	12.77	1620
Te L	**13.52**	**3.43**	450
Totals	**100.00**	**100.00**	

Figure 4.6: SEM-image (left) and EDX (right) of the final $Mo_1V_{0.3}Te_{0.23}Nb_{0.12}O_x$ catalyst pre-calcine at 598 K and calcine at 873 K under argon.

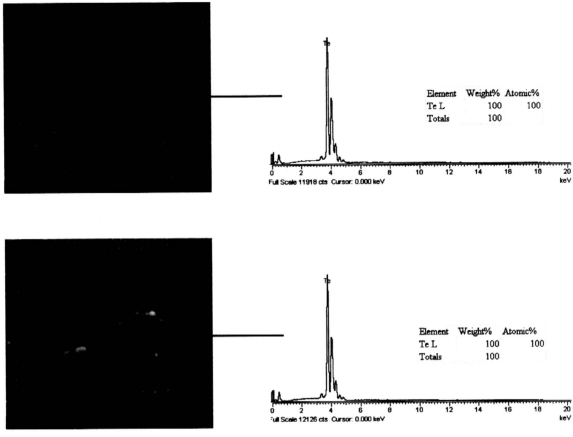

Figure 4.7: SEM-image (left) and EDX (right) of the tellurium metal evaporated when the $Mo_1V_{0.3}Te_{0.23}Nb_{0.12}O_x$ catalyst was calcine at temperature 873 K under argon.

b) Effects of Viscosity Enhancer

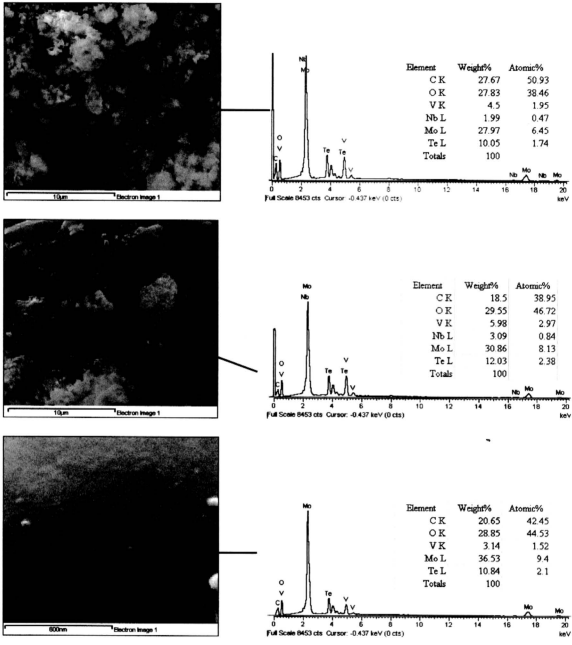

Element	Weight%	Atomic%	Melting point (^{O}C)
O K	33.95	73.56	-
V K	8.19	5.65	1915
Nb L	5.64	2.13	2468
Mo L	46.72	17.07	1620
Te L	**5.51**	**1.60**	450
Totals	**100.00**	**100.00**	

Figure 4.8: SEM-image (left) and EDX (right) of the final $Mo_1V_{0.3}Te_{0.23}Nb_{0.12}O_x$ catalyst adding PEG as a viscosity enhancer.

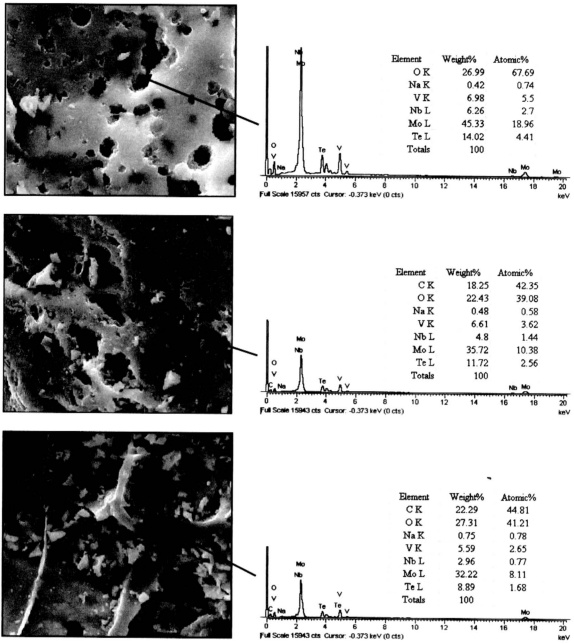

Element	Weight%	Atomic%	Melting point (^{O}C)
O K	30.32	71.00	-
V K	7.08	5.33	1915
Nb L	5.79	2.39	2468
Mo L	43.06	17.15	1620
Te L	**13.77**	**4.14**	450
Totals	**100.00**	**100.00**	

Figure 4.9: SEM-image (left) and EDX (right) of the final $Mo_1V_{0.3}Te_{0.23}Nb_{0.12}O_x$ catalyst adding HEC as a viscosity enhancer.

C) Effect of Precursor

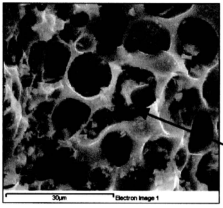

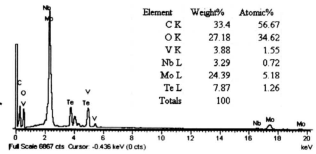

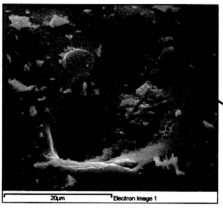

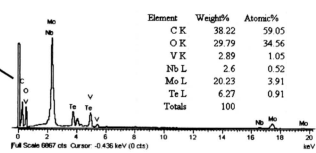

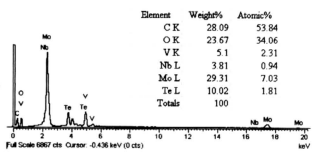

Element	Weight%	Atomic%	Melting point (^{O}C)
O K	31.34	72.49	-
V K	6.42	4.68	1915
Nb L	6.08	2.43	2468
Mo L	42.12	16.31	1620
Te L	**14.05**	**4.09**	450
Totals	**100.00**	**100.00**	

Figure 4.10: SEM-image (left) and EDX (right) of the final $Mo_1V_{0.3}Te_{0.23}Nb_{0.12}O_x$ catalyst prepared via citric acid route with ratio 1:1 metal to citric acid.

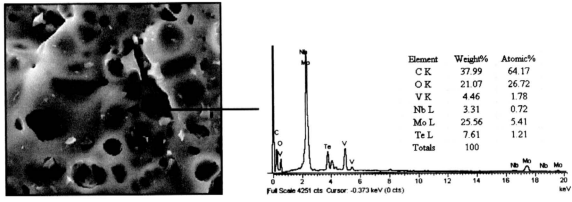

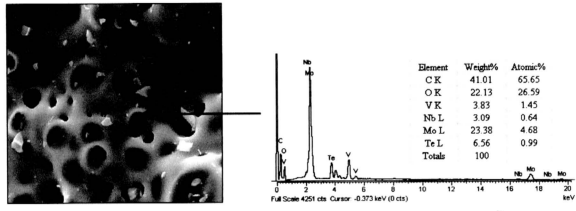

Element	Weight%	Atomic%	Melting point (^{O}C)
O K	23.10	62.79	-
V K	9.61	8.24	1915
Nb L	6.30	2.96	2468
Mo L	45.69	20.77	1620
Te L	**15.29**	**5.24**	450
Totals	**100.02**	**100.00**	

Figure 4.11: SEM-image (left) and EDX (right) of the final $Mo_1V_{0.3}Te_{0.23}Nb_{0.12}O_x$ catalyst prepared via citric acid route with ratio 1:2 metal to citric acid.

4.3 Structural & Morphology Study

4.3.1 Unpromoted Mo-V-Te-Nb-Ox catalyst system

a) Effect of Pre-Calcine Temperature

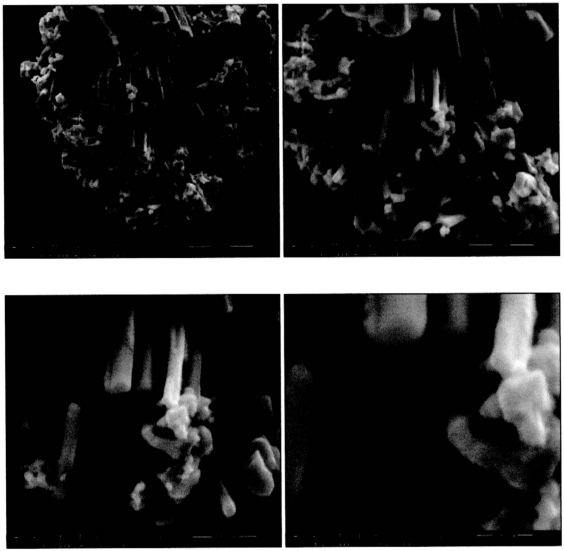

Figure 4.12: SEM-image of the final $Mo_1V_{0.3}Te_{0.23}Nb_{0.12}O_x$ catalyst prepared by slurry method, pre-calcine at 448 K and calcine at 873 K under argon.

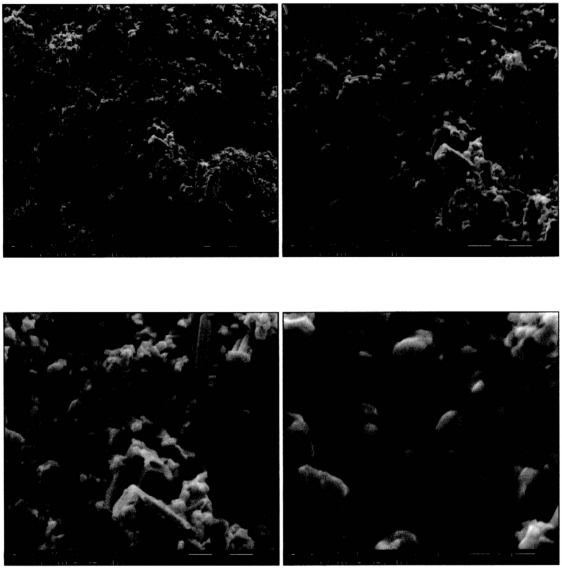

Figure 4.13: SEM-image of the final $Mo_1V_{0.3}Te_{0.23}Nb_{0.12}O_x$ catalyst prepared by slurry method, pre-calcine at 498 K and calcine at 873 K under argon.

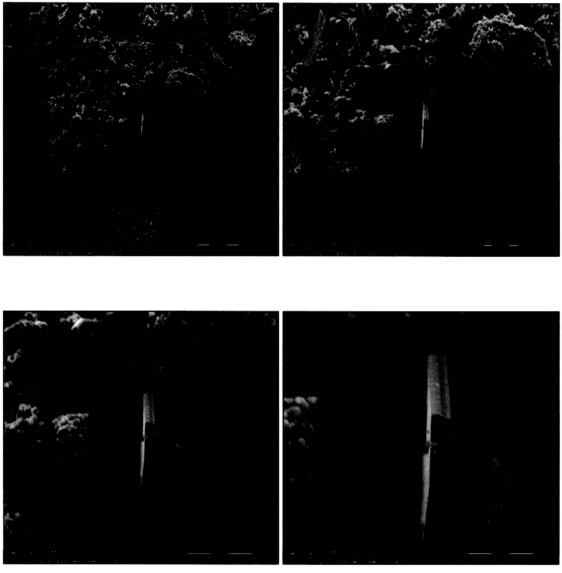

Figure 4.14: SEM-image of the final $Mo_1V_{0.3}Te_{0.23}Nb_{0.12}O_x$ catalyst prepared by slurry method, pre-calcine at 548 K and calcine at 873K under argon.

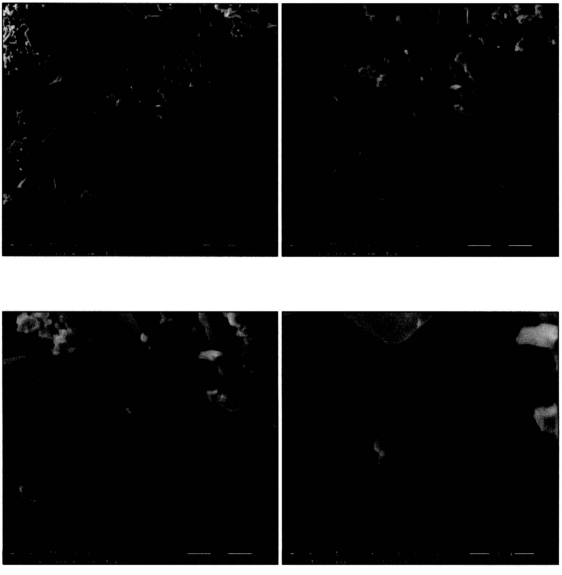

Figure 4.15: SEM-image of the final $Mo_1V_{0.3}Te_{0.23}Nb_{0.12}O_x$ catalyst prepared by slurry method, pre-calcine at 598 K and calcine at 873 K under argon.

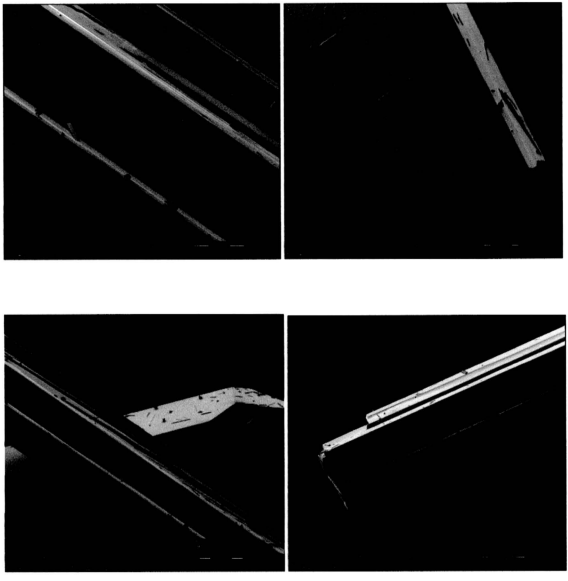

Figure 4.16: SEM-image of tellurium metal evaporated when the $Mo_1V_{0.3}Te_{0.23}Nb_{0.12}O_x$ catalyst was calcine at temperature 873 K under flow of argon.

b) Effect of Viscosity Enhancer

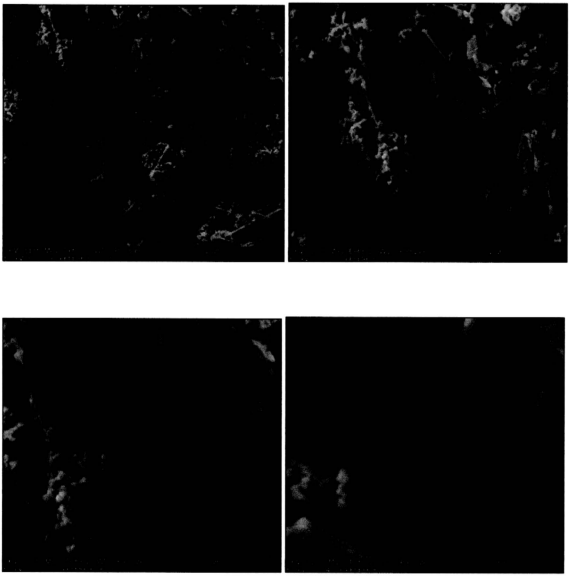

Figure 4.17: SEM-image of the final $Mo_1V_{0.3}Te_{0.23}Nb_{0.12}O_x$ catalyst prepared by slurry method adding PEG as a viscosity enhancer.

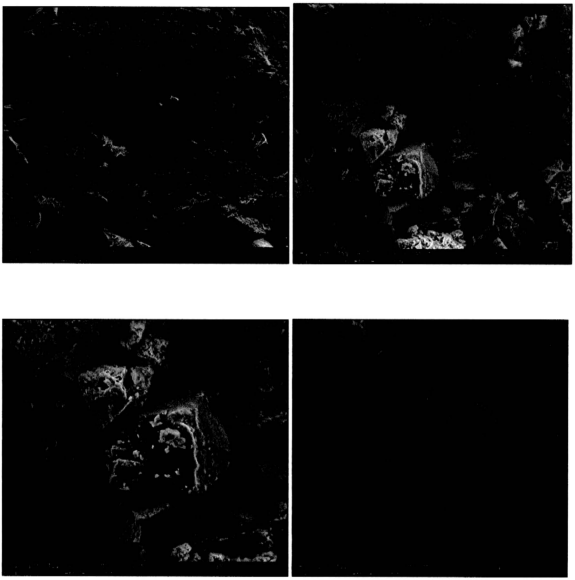

Figure 4.18: SEM-image of the final $Mo_1V_{0.3}Te_{0.23}Nb_{0.12}O_x$ catalyst prepared by slurry method adding HEC as a viscosity enhancer.

c) Effect of Precursor

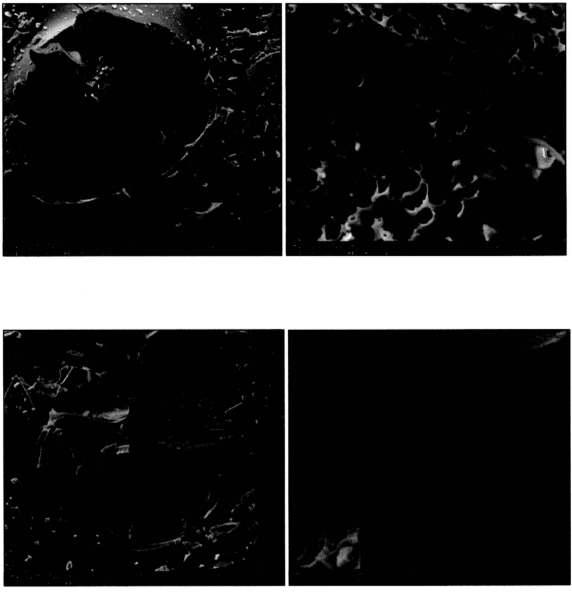

Figure 4.19: SEM-image of the final $Mo_1V_{0.3}Te_{0.23}Nb_{0.12}O_x$ catalyst prepared via citric acid route with ratio 1:1 metal to citric acid.

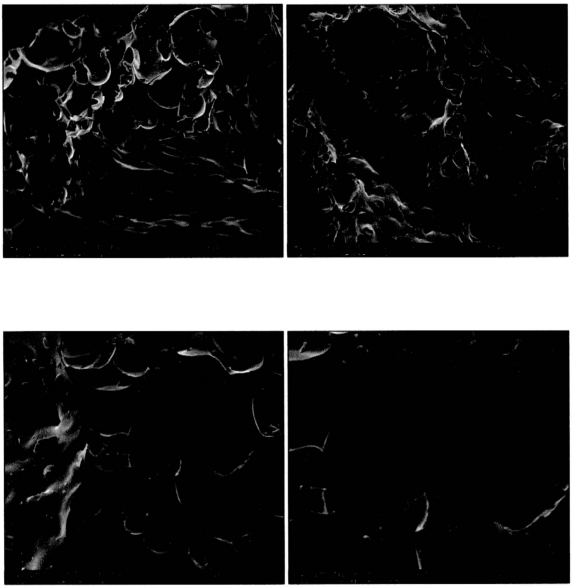

Figure 4.20: SEM-image of the final $Mo_1V_{0.3}Te_{0.23}Nb_{0.12}O_x$ catalyst prepared via citric acid route with ratio 1:2 metal to citric acid.

Element Composition & Surface Morphology Discussion

The extensive investigation of morphology and local chemical composition is complied in the Figures *4.3* to *4.32* are refer to EDX and SEM image. Table 4.5 to 4.8 are referring to the quantitative of element composition. The low-magnification SEM images reveal a coarsely granular structure typical of a mixture of well-shaped crystals for the majority of samples.

The samples prepared from citric acid and prepared with the addition of viscosity enhancers (*see Figures 4.17, 4.18, 4.19, and 4.20)* exhibit a grossly different morphology. They were transformed in a topotactic fashion from the spherical gel precursor with a large number of macrospores being formed in the drying and partial ligand oxidation process. It is clear from the pore structure that the appearance of these samples is a replica of the morphology of the precursor state of all the samples. For a chemical reason the precursor was not transformed into its final phase mixture characteristic of all other samples.

The EDX data show that a great deal of the large support structure seen in particular with the citrate samples is indeed active carbon stemming form carbonisation rather than oxidation of the organic ligand material during pre-calcination. It is clear that the oxygen partial pressure was largely insufficient to remove the ligand system in the pre-calcination process. The formation of carbonisation products may have preserved the gel morphology. During main calcination the possible auto reduction of the oxides by carbon did not occur due to insufficient dispersion of the carbon the oxide phase and due to insufficient heating time. In this way the strongly different micromorphology of the organic-rich samples can be rationalised.

The pre-calcination left also in the other cases sufficient reducing material to cause a systematic deviation of the oxide mixture from structures with the highest oxidation states of the Mo and V –containing solids. Both, the Anderson phase (Mo-tellurate) and the V-molybdate are under stoichiometric in oxygen and crystallise as sub-oxides only under reducing conditions [74]. The EDX analysis apparently contradicts this as exemplified from the data of *Figure 4.3* measured oxygen content 75.63 atomic %, expected for a composition with maximum oxidation state: 68.84 atomic %. The discrepancy is easily explained when we look at the thermal analysis section where a large content of crystal and hydration water is found that outnumbers the possible deficit in oxygen content by about an order of magnitude in atomic %.

EDX can thus only in cationic compositional ratios be used to identify the morphologies with crystal structures. A real chemical analysis in terms of phase and oxide deficiency is not possible. This limited analytical relevance of EDX led to the tabulation of results in typical cation ratios rather than in chemical formula.

A correlation of M1, M2 cationic composition with the two prevailing morphologies of platelets and agglomerates identifies clearly the platelets as the Anderson phase and the agglomerate as the morphology of the other phases. It is highly significant that most of the platelets contain a small amount of non-stoichiometric impurity of vanadium but with no Nb. The molybdenum tellurate is thus a pseudo-ternary vanado-molybdo-tellurate and the agglomerate may be formed of two phases namely of the vanadium-molybdate and of the M1/M2 phases.

4.2.1 Promoted Mo-V-Te-Nb-Ox catalyst system

a) Effect of Nickel Promoter

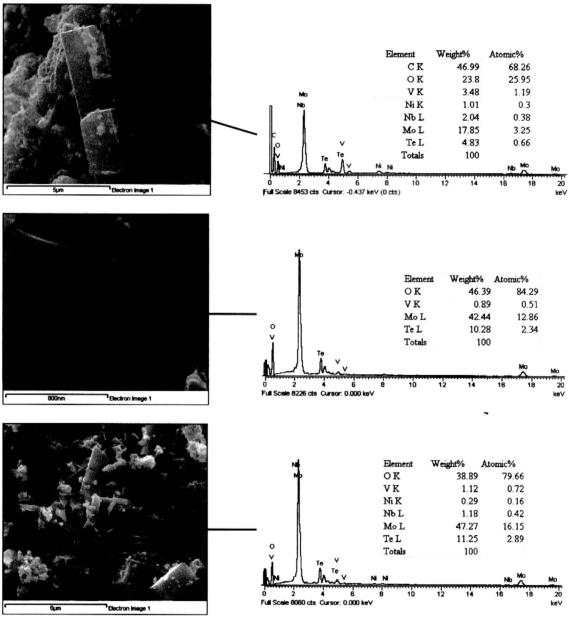

Element	Weight%	Atomic%	Melting point (^{O}C)
O K	43.99	81.45	-
V K	4.82	2.83	1915
Ni K	1.16	0.58	1455
Nb L	3.45	1.12	2468
Mo L	37.53	11.86	1620
Te L	**9.06**	**2.15**	450
Totals	**100.02**	**99.98**	

Figure 4.21: SEM-image (left) and EDX (right) of the final $Mo_1V_{0.3}Te_{0.23}Nb_{0.12}O_x$ catalyst system adding nickel as a promoter with weight loading 0.05 atomic percent.

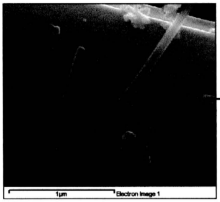

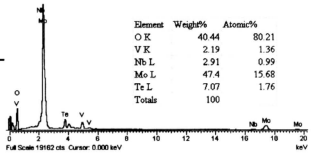

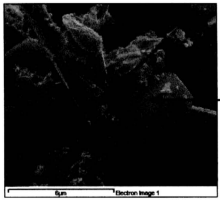

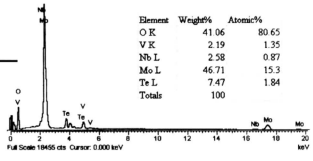

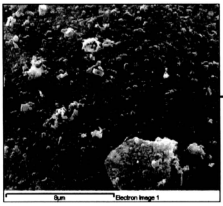

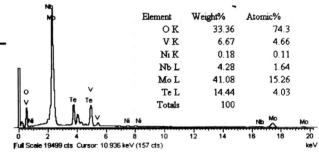

Element	Weight%	Atomic%	Melting point (^{O}C)
O K	38.49	78.54	-
V K	**4.08**	**2.68**	**1915**
Ni K	0.05	0.03	1455
Nb L	2.93	1.04	**2468**
Mo L	43.92	14.97	1620
Te L	**10.54**	**2.74**	450
Totals	**100.00**	**100.0**	

Figure 4.22: SEM-image (left) and EDX (right) of the final $Mo_1V_{0.3}Te_{0.23}Nb_{0.12}O_x$ catalyst system adding nickel as a promoter with weight loading 0.005 atomic percent.

b) Effect of Chromium Promoter

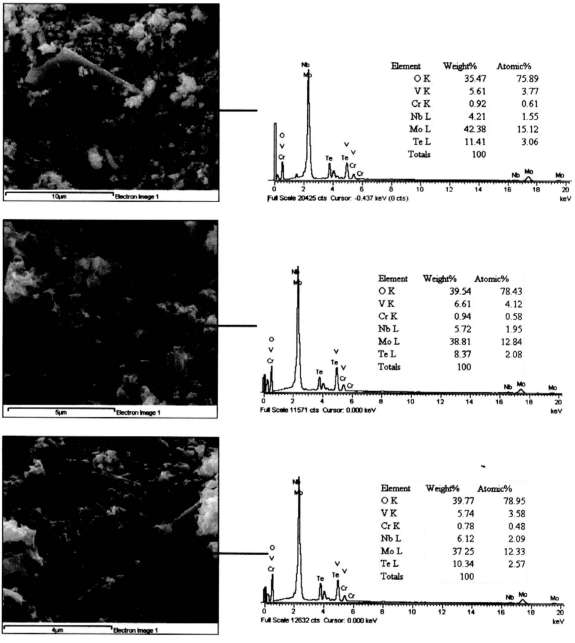

Element	Weight%	Atomic%	Melting point (^{O}C)
O K	36.06	75.99	-
V K	6.30	4.20	1915
Cr K	0.96	0.63	1900
Nb L	5.32	1.93	2468
Mo L	40.70	14.41	1620
Te L	**10.65**	**2.84**	450
Totals	**100**	**100.0**	

Figure 4.23: SEM-image (left) and EDX (right) of the final $Mo_1V_{0.3}Te_{0.23}Nb_{0.12}O_x$ catalyst system adding chromium as a promoter with weight loading 0.05 atomic percent.

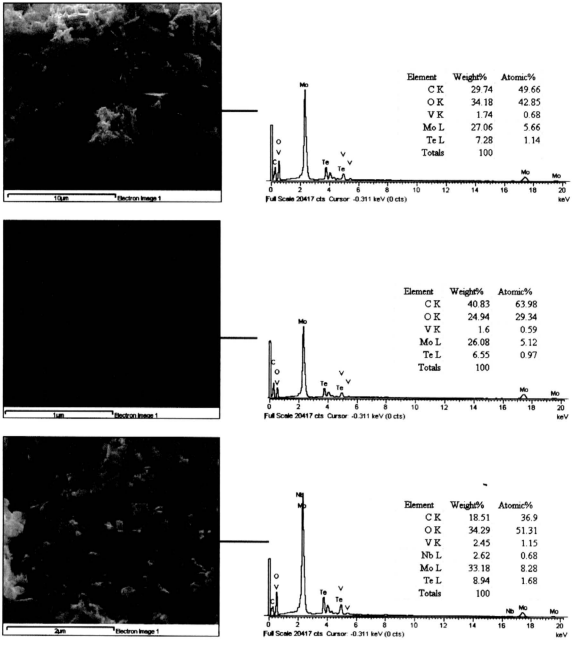

Element	Weight%	Atomic%	Melting point (^{O}C)
O K	38.25	78.45	-
V K	3.95	2.60	1915
Cr K	2.65	0.93	1900
Nb L	42.96	14.84	2468
Mo L	12.19	3.18	1620
Te L	**38.25**	**78.45**	450
Totals	**99.99**	**100.00**	

Figure 4.24: SEM-image (left) and EDX (right) of the final $Mo_1V_{0.3}Te_{0.23}Nb_{0.12}O_x$ catalyst system adding chromium as a promoter with weight loading 0.005 atomic percent.

c) Effect of Cobalt Promoter

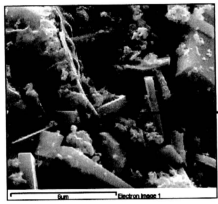

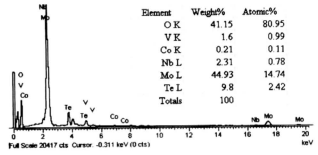

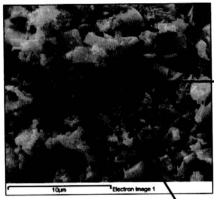

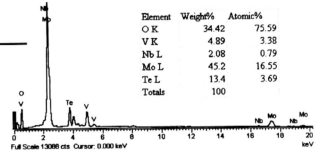

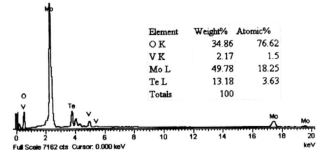

Element	Weight%	Atomic%	Melting point (^{O}C)
O K	41.55	80.84	-
V K	2.86	1.78	1915
Co K	0.43	0.23	1495
Nb L	2.09	0.72	2468
Mo L	41.39	13.56	1620
Te L	**11.68**	**2.88**	450
Totals	**100.00**	**100.00**	

Figure 4.25: SEM-image (left) and EDX (right) of the final $Mo_1V_{0.3}Te_{0.23}Nb_{0.12}O_x$ catalyst system adding cobalt as a promoter with weight loading 0.05 atomic percent.

c) Effect of Cobalt Promoter

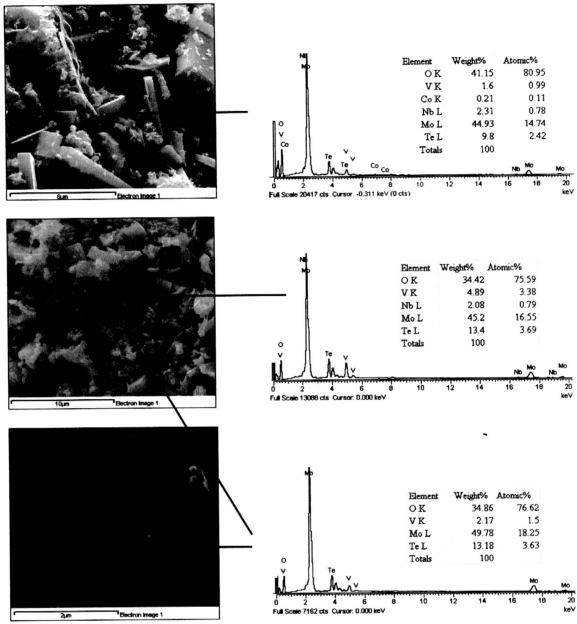

Element	Weight%	Atomic%	Melting point (^{O}C)
O K	41.55	80.84	-
V K	2.86	1.78	1915
Co K	0.43	0.23	1495
Nb L	2.09	0.72	2468
Mo L	41.39	13.56	1620
Te L	**11.68**	**2.88**	450
Totals	**100.00**	**100.00**	

Figure 4.25: SEM-image (left) and EDX (right) of the final $Mo_1V_{0.3}Te_{0.23}Nb_{0.12}O_x$ catalyst system adding cobalt as a promoter with weight loading 0.05 atomic percent.

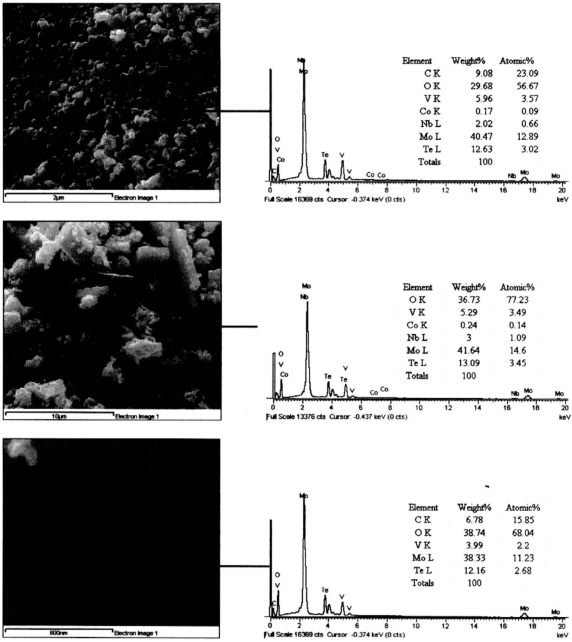

Element	Weight%	Atomic%	Melting point (^{O}C)
O K	34.69	75.46	-
V K	5.92	4.07	1915
Co K	0.21	0.13	1495
Nb L	2.61	0.97	2468
Mo L	43.08	15.68	1620
Te L	**13.49**	**3.69**	450
Totals	**100.01**	**100.00**	

Figure 4.26: SEM-image (left) and EDX (right) of the final $Mo_1V_{0.3}Te_{0.23}Nb_{0.12}O_x$ catalyst system adding cobalt as a promoter with weight loading 0.005 atomic percent.

Table 4.5: Bulk atomic ratio of final $Mo_1V_{0.3}Te_{0.23}Nb_{0.12}O_x$ catalyst prepared by slurry method and pre-calcine at various temperatures and phase M1 and M2 from literature review [73].

Catalyst	Phase (from XRD)	Atomic Ratio				
		V / Mo	Nb /Mo	Te / Mo	Te / (Mo + V + Nb)	(Te + Nb) / (Mo + V)
M1	M1	0.30	0.07	0.32	0.23	
M2	M2	0.23	0.14	0.11	0.08	0.20
MoVTeNbOx (I)	M2 + $TeMo_5O_{16}$ + $V_{0.95}Mo_{0.97}O_5$	0.28	0.11	0.13	0.09	0.19
MoVTeNbOx (II)	M2 + $TeMo_5O_{16}$ + $V_{0.95}Mo_{0.97}O_5$	0.19	0.08	0.17	0.14	0.22
MoVTeNbOx (III)	M2 + $TeMo_5O_{16}$ + $V_{0.95}Mo_{0.97}O_5$	0.4	0.15	0.25	0.16	0.29
MoVTeNbOx (IV)	M2 + $TeMo_5O_{16}$ + $V_{0.95}Mo_{0.97}O_5$	0.3	0.09	0.27	0.19	0.28

MoVTeNbOx (I): Catalyst pre-calcine at 448 K and calcine at 873 K under argon.
MoVTeNbOx (II): Catalyst pre-calcine at 498 K and calcine at 873 K under argon.
MoVTeNbOx (III): Catalyst pre-calcine at 548 K and calcine at 873 K under argon.
MoVTeNbOx (IV): Catalyst pre-calcine at 598 K and calcine at 873 K under argon.

Table 4.6: EDX analysis of final $Mo_1V_{0.3}Te_{0.23}Nb_{0.12}O_x$ catalyst prepared by slurry method adding PEG or HEC as a viscosity enhancer

Catalyst	Phase (from XRD)	Atomic Ratio				
		V / Mo	Nb /Mo	Te / Mo	Te / (Mo + V + Nb)	(Te + Nb) / (Mo + V)
MoVTeNbOx + PEG	None crystalline phase	0.33	0.12	0.09	0.06	0.16
MoVTeNbOx + HEC	None crystalline phase	0.31	0.14	0.24	0.17	0.29

MoVTeNbOx (I): Catalyst adding polyethylene glycol (PEG) as a viscosity enhancer.
MoVTeNbOx (II): Catalyst adding Hydroxyl ethyl cellulose (HEC) as a viscosity enhancer.

Table 4.7: EDX analysis of final $Mo_1V_{0.3}Te_{0.23}Nb_{0.12}O_x$ catalyst prepared via citric acid route with two different ratios.

Catalyst	Phase (from XRD)	Atomic Ratio				
		V / Mo	Nb /Mo	Te / Mo	Te / (Mo + V + Nb)	(Te + Nb) / (Mo + V)
MoVTeNbOx (1:1)	None crystalline phase	0.29	0.15	0.25	0.17	0.31
MoVTeNbOx (1:2)	None crystalline phase	0.4	0.14	0.25	0.16	0.28

MoVTeNbOx (1:1): Catalyst prepared with ratio 1:1 metal to citric acid.
MoVTeNbOx (1:2): Catalyst prepared with ratio 1:2 metal to citric acid.

Table 4.8: EDX analysis of final promoted $Mo_1V_{0.3}Te_{0.23}Nb_{0.12}O_x$ catalyst prepared by slurry method with two different weight loading.

Catalyst	Phase (from XRD)	Atomic Ratio				
		V / Mo	Nb /Mo	Te / Mo	Te / (Mo + V + Nb)	(Te + Nb) / (Mo + V)
MoVTeNbOx Ni (I)	M2 + $TeMo_5O_{16}$ + $V_{0.95}Mo_{0.97}O_5$	0.24	0.009	0.18	0.14	0.22
MoVTeNbOx Ni (II)	M2 + $TeMo_5O_{16}$ + $V_{0.95}Mo_{0.97}O_5$	0.18	0.07	0.18	0.15	0.21
MoVTeNbOx Cr (I)	M2 + $TeMo_5O_{16}$ + $V_{0.95}Mo_{0.97}O_5$	0.29	0.13	0.2	0.14	0.26
MoVTeNbOx Cr (II)	M2 + $TeMo_5O_{16}$ + $V_{0.95}Mo_{0.97}O_5$	0.18	0.006	0.21	0.17	0.24
MoVTeNbOx Co (I)	M2 + $TeMo_5O_{16}$ + $V_{0.95}Mo_{0.97}O_5$	0.13	0.05	0.21	0.18	0.23
MoVTeNbOx Co (II)	M2 + $TeMo_5O_{16}$ + $V_{0.95}Mo_{0.97}O_5$	0.26	0.06	0.24	0.18	0.24

MoVTeNbOx Ni (I) : Catalyst adding Ni as a promoter with weight loading 0.05 atomic weight.
MoVTeNbOx Ni (II) : Catalyst adding Ni as a promoter with weight loading 0.005 atomic weight..
MoVTeNbOx Cr (I) : Catalyst adding Cr as a promoter with weight loading 0.05 atomic weight.
MoVTeNbOx Cr (II) : Catalyst adding Cr as a promoter with weight loading 0.005 atomic weight.
MoVTeNbOx Co (I) : Catalyst adding Co as a promoter with weight loading 0.05 atomic weight.
MoVTeNbOx Co (II) : Catalyst adding Co as a promoter with weight loading 0.005 atomic weight.

4.3.2 Promoted Mo-V-Te-Nb-Ox catalyst system

a) Effect of Nickel Promoter

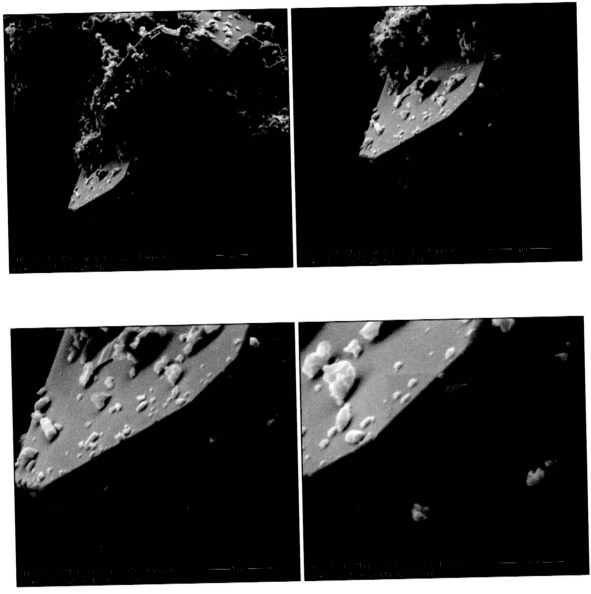

Figure 4.27: SEM-image of the final promoted $Mo_1V_{0.3}Te_{0.23}Nb_{0.12}Ni_{0.05}O_x$ catalyst prepared by slurry method adding nickel with weight loading 0.05 as a promoter.

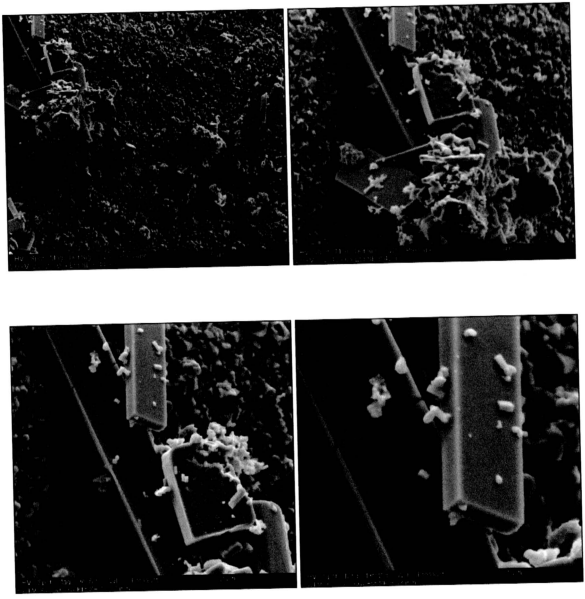

Figure 4.28: SEM-image of the final promoted $Mo_1V_{0.3}Te_{0.23}Nb_{0.12}Ni_{0.005}O_x$ catalyst prepared by slurry method adding nickel with weight loading 0.005 as a promoter.

c) Effect of Chromium Promoter

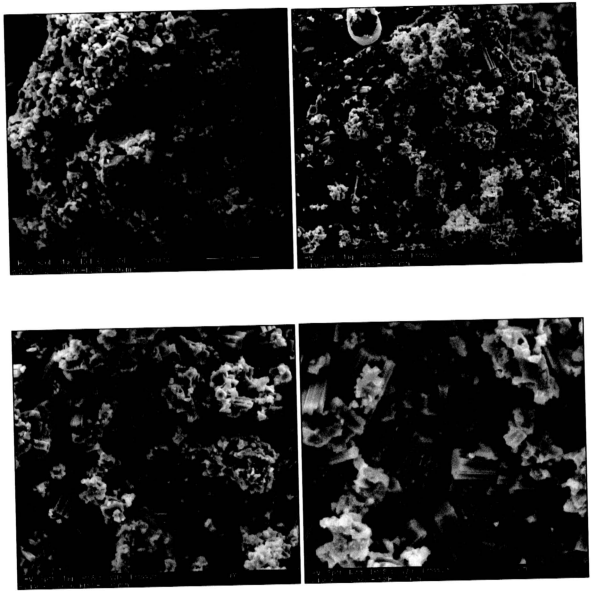

Figure 4.29: SEM-image of the final promoted $Mo_1V_{0.3}Te_{0.23}Nb_{0.12}Cr_{0.05}O_x$ catalyst prepared by slurry method adding chromium with weight loading 0.05 as a promoter.

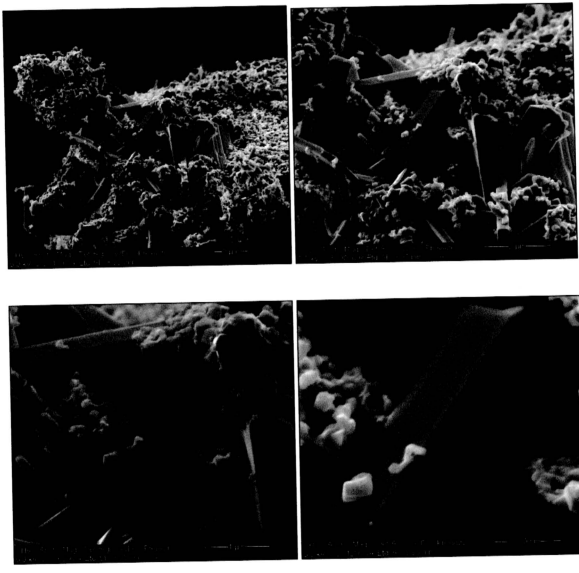

Figure 4.30: SEM-image of the final promoted $Mo_1V_{0.3}Te_{0.23}Nb_{0.12}Cr_{0.005}O_x$ catalyst prepared by slurry method adding chromium with weight loading 0.005 as a promoter.

c) Effect of Cobalt Promoter

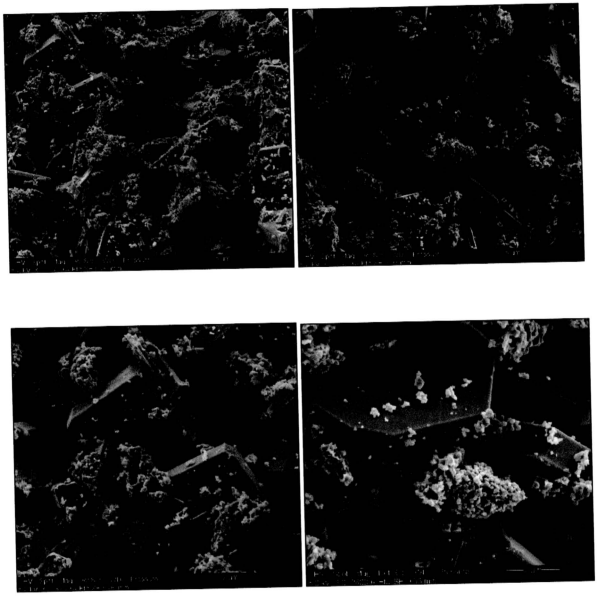

Figure 4.31: SEM-image of the final promoted $Mo_1V_{0.3}Te_{0.23}Nb_{0.12}Co_{0.05}O_x$ catalyst prepared by slurry method adding cobalt with weight loading 0.05 as a promoter.

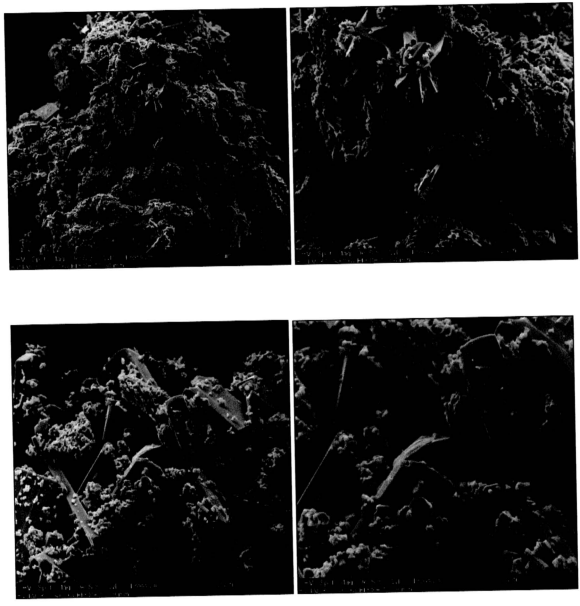

Figure 4.32: SEM-image of the final promoted $Mo_1V_{0.3}Te_{0.23}Nb_{0.12}Co_{0.005}O_x$ catalyst prepared by slurry method adding cobalt with weight loading 0.005 as a promoter.

Two exceptions to this morphology assignment are noted; i) The Cr promoter is fully homogeneously distributed over all particles and exhibits no enrichment in any discernible segregation. ii) The Ni promoter, on the contrary is ex-soluted from the platelets and forms surface aggregates of probably NiO on their surfaces. Ni is definitely not co-substituted with V for Mo in the Anderson phase.

The carbon-supported materials (*Figure 4.17 & 4.18*) are exceptionally homogeneous also in their chemical composition indicating that the polycondensation of the gel precursor was due to the carbonisation rather than oxidation of the ligands, too rapid to allow spatial re-organisation and that these materials preserve as oxides the elemental dispersion of the solution down to the nano-dimension: They are supported "petrified" precursors and did not undergo structural and textural formation in size scales resolved by SEM. This finding agrees well with the XRD amorphous character of the oxides.

The micromorphology of the precalcination series is characterised by the co-existence of three different morphologies: At low calcination temperature needles (*Figure 4.12*); they formed are shorten at medium temperatures (*Figure 4.13*) and degenerate to platelets above 548 K (*Figure 4.14 & Figure 4.15*). A featureless glue phase can be seen in all images covering the large objects and binding small crystallites forming complex aggregates as third morphology. This glue phase appears as fragment from outer agglomerates in some of the low magnification images as compact featureless platelets. The aggregate phase seems to become gradually less abundant in high-temperature calcination samples. The fact that the glue phase can be seen on both large-scale regular objects (platelets and needles) and on the agglomerates indicates that the two-regular-shaped morphologies are formed first and that the glue phase that must be of different chemical composition than the rest is formed last. The lack of

porosity except that of intergranular pores further indicates that all the microstructure seen in the SEM has been formed after the pre-calcination step where large amounts of gas have evolved. This observation is fully consistent with the XRD observations showing X-ray amorphous materials after the pre-calcination.

In-general the multiple morphology accounts for the surface area and is to be expected from a multi-phase character of the MoVTe system. It is evident that the optimisation of the pre-calcination procedure coincides with the morphology change from needles to platelets.

It is further significant that some of the Te is lost during calcination. The needles of elemental Te can be seen in *Figure 4.7* for EDX result and *Figure 4.16* for SEM result. This happens as Te evaporates as a metal couple with a strong indication for insufficient pre-calcination. This loss of Te may be avoided if a suitable oxygen partial pressure would be preserved in the main calcination phase over the decomposing Te-acid or TeO_2. This is not possible in the presence of organic reducing species and their presence lead thus inevitably to the thermal decomposition of Te compounds leaving behind sub-oxides and metallic Te.

The micro morphology of the promoted samples (*Figures 4.31 & 4.32*) shows little general deviation from the morphology mix of the unpromoted samples. The only clear exception is the case of Ni promotion where a separate nanostructured NiO phase is discernible on the platelets of the molybdo-tellurate phase. The absence of any such segregation of the Cr promoter despite its proven elemental presence by EDX is a confirmation of the expected high dispersion of Cr in the molybdate matrix. This is the consequence of the chemical similarity of Cr and V that are as early transition metals electronically more compatible with the molybdate matrix than the later transition

metals Ni and Co whose cohesion energy in binary oxides is a driver for separate phase formation in an electron-rich matrix of molybdo-tellurates.

In summary, the SEM-EDX analysis has revealed the multi-phase nature of the MoVTe samples. It has further confirmed that the phase formation occurs kinetically after the gas evolution of the ligand removal. In some cases the ligand removal did not happen. The pre-calcination led to a carbon-inorganic composite material with maybe interesting but non-catalytic properties. The promotion had little morphological effect besides separate phase formation of the later transition metal oxides.

The EDX analysis in general and the correlation with XRD in particular (*See Table 4.5*) shows that the pre-calcination step was inadequately conducted within the goal of removing all reducible species prior to catalytic phase formation. The fact that apparently compact oxide crystals still contain large elemental excess of oxygen as water is an indication that there is a hierarchy of structures with the nanostructural details not being seen with the SEM. It can be expected that after high-temperature treatment (e.g. in operation conditions) there will be a significant number of voids and defects present in crystals that appear completely flat and smooth at ambient conditions of SEM observation. In conclusion the thermal treatment of the precursor gel will require much improvement in optimisation of temperature levels, time profiles and chemical composition to allow the idea of converting a ligand-containing gel of the MoVTe composition into a mixed oxide with a majority of material exhibiting the M1 composition and structure.

4.4 Powder X-ray diffraction

Powder XRD is used to identify the phase inventory of the catalysts. From literature (*Grasselli, Millet, Lopez & Ueda et al.)* [51, 53, 73-77], it is known that the successful catalyst should be a mixture of two phases namely of an orthorhombic and a hexagonal variant of the MoVTeNb system referred to as M1 and M2 phases. As different authors use different designations for the same phase we refer to ortho and hex as unambiguous designations. In addition, it is known that a third phase known as "Andersson Mo-tellurate" crystallizing in rutile and triclinic variants can also be present. Finally, several V-substituted Mo oxides namely Mo_5O_{14} and several MoVOx phases of Magnelli type structures have been mentioned as possible constituents.

Of key relevance for the function is the ortho phase. Without its presence there is little catalytic activity in propane to acrylic acid conversion. Synthesis of a reference material was performed according to the standard prescription described earlier with the reference composition and with spray-drying as solidification technique. The dried pre-catalyst was carefully pre-calcined in air at 548 K until all reducible species were removed followed by an inert calcination to 898 K. This procedure yielded a reference material consisting of the ortho phase with a small admixture of the hex phase very much as the most successful catalyst (E) in Figure 4 [75]. Figure 4.33 shows the experimental pattern together with a simulated diffraction data set obtained from the Rietveldt analysis of Grasselli and Bouttrey.

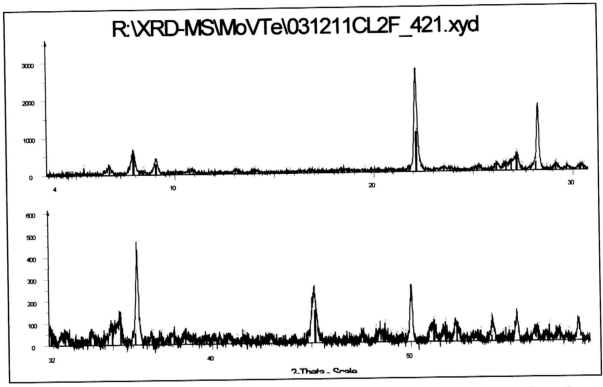

Figure 4.33: The experimental pattern with a simulated diffraction data set from the Rietveldt analysis (Grasselli and Bouttrey et al.) [75].

It can be seen that a fairly "clean" diffraction pattern is obtained with a very characteristic triplet of reflections occurring around 8 deg for Cu radiation.

In the discussion of the literature XRD patterns it is commonly said that $Mo_1V_{0.3}Te_{0.23}Nb_{0.12}O_x$ catalyst samples should present strong Bragg reflection at 2θ = 22.1, 28.2, 36.2, 45.2, and 50.0 ("famous five"). These famous five lines suggest as fingerprint the formation of a recently reported Te-V-Mo-O or Te-V-Nb-Mo-O (TeMO) crystalline phase designated as "M1" in the Grasselli work [75, 76]. The selection of peaks characterizes in fact mixture of ortho and of hex phase for about 80% of the total intensity of these lines indicating the hex phase as can be seen from Figure 4.33. The low-angle reflections arising from the (020), (120) and (210) lattice planes of the ortho phase are rarely mentioned in the literature although clearly visible in diffraction patterns from the literature of some successful catalyst preparations. In the

majority of literature data the lines are, however, absent or very weak indicating that only or none of the ortho phase is present. The "famous five" lines are thus indicating primarily the formation of hex phase. The Andersson phase ammonium hexamolybdotellurate phase, $(NH_4)_6(TeMo_6O_{24}) \cdot 7H_2O$, was detected for all dried material and for the pre-calcined material only as poorly crystalline phase (*Nieto et al).* [51]. From most XRD patterns it occurs that $Mo_1V_{0.3}Te_{0.23}Nb_{0.12}O_x$ should be present using the famous five strong Bragg reflection at 2θ = 22.1, 28.2, 36.2, 45.2, and 50.0 as indicators. This suggests the formation of a recently reported Te-V-Mo-O or Te-V-Nb-Mo-O (TeMO) crystalline phase [78, 79].

The key crystal structures may be described in the following way. The TeMO phase, with a stoichiometry of $Te_{0.33}Mo_{0.75}V_{0.25-x}Nb_xO_z$ ($0 < x < 0.25$), is from its structural motif similar to the hexagonal tungsten bronze ($K_{0.13\ -\ 0.33}\ WO_3$) or to $Sb_{0.4}MoO_{0.31}$ [79] and could correspond to the phase-*M2* proposed by *Ushikubo et al.* [80] and to the phase –*M1* proposed by Aouine and Dubois *et al.* [73]. The *M1* phase was reported as orthorhombic with space group $P2_12_12$ and cell parameters a = 21.207Å, b = 26.831Å and c = 8.047Å. Millet *et al.* [53] suggested that the *M1* phase was isostructural with $Cs_{0.7}(Nb_{2.7}W_{2.3})O_{14}$ [81], and Aouine *et al.* [73] suggested that *M2* phase was isolated with $Sb_{0.4}MoO_{0.31}$[82]. This *M2* phase was found to be hexagonal with possible space group *P*6mm, *P*-6m2, *P*622, or *P*6/mmm and cell parameters a=28.74 Å and c=4.03 Å, where *M1* and *M2* phases are proposed as active for selective oxidation process. Figures 4.34, 4.35 and 4.36 show the atomic structure of *M1*, *M2* and $(NH_4)_6(TeMo_6O_{24}) \cdot 7H_2O$ phase. The following Figures present views of some key structures.

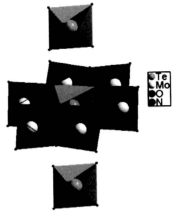

Figure 4.34: Structure of ammonium hexamolybdotellurate phase, $(NH_4)_6(TeMo_6O_{24}) \cdot 7H_2O$ "Andersson phase" from MoVTeNbOx dried sample (Nieto et al.) [51]

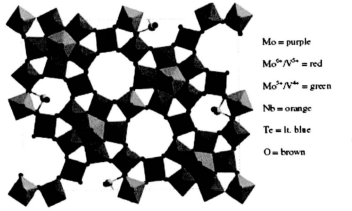

Figure 4.35: Average phase of M1 $Mo_{0.75}V_{1.5}NbTeO_{29}$ [75].

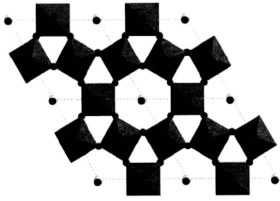

Figure 4.36: Subunit cell structure model of pseudohexagonal $Mo_6Te_2VO_{24}$ (M2) phase (p6mm:a=14.5846 Å, c=4.0207 Å) in [001] projection [75].

It occurs that the Anderson phase is a typical molybdate structure derived from molecular heptamolybdate with a cluster of octahedral grouped around a structure-forming central Te-unit. The ortho and hex phases, however, are different from most molybdates in as much as they contain the pentagonal bipyramid surrounded by 5 octahedral as supramolecular building block. The interconnection of these units is different for the two phases giving rise to clearly differing channel systems seen prominently in the Figures 4.35 and 4.36. In ortho (*Figure 4.35*), three octahedral link low clusters whereas in the hex phase (*Figure 4.36*) a more densely linking with only one octahedron is realized. It should be noted that the Mo_5O_{14} structure contains also this structural motif with 4 interlinking octahedral. It seems very likely that the existence of the supramolecular motif is a necessary structural requirement for catalytic function but it is also clear that this is not sufficient as otherwise the admixture of at least two of these phases which is viewed according to the "pillars for selective oxidation" an indispensable condition for a good catalytic material would be unnecessary for high performance.

In the following, we investigate the evolution of the different phases as a function of chemical and treatment variables.

4.4.1 Unpromoted Mo-V-Te-Nb-Ox Catalyst System.

a) Effect of Pre-Calcination Temperature

Figures 4.37 show the X-ray powder diffraction (XRD) patterns for dry sample, pre-calcined sample and calcined sample of unpromoted $Mo_1V_{0.3}Te_{0.23}Nb_{0.12}O_x$ catalysts system prepared by various precalcined temperature (448 K, 498 K, 548 K and 598 K) with the precursor composition of the catalysts being kept constant at $Mo_1V_{0.3}Te_{0.23}Nb_{0.12}O_x$.

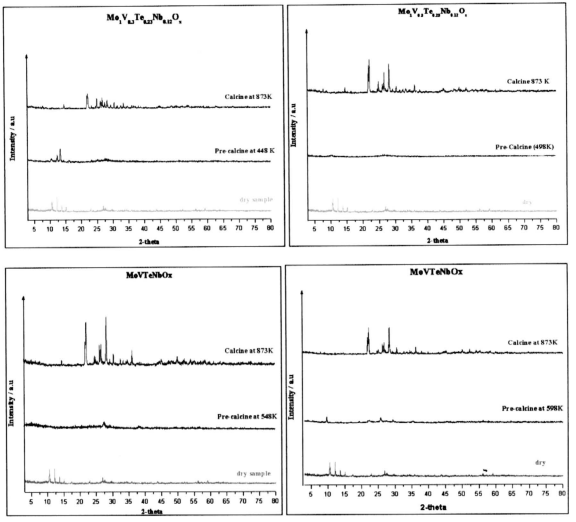

Figure 4.37: X-ray diffraction patterns of unpromoted $Mo_1V_{0.3}Te_{0.23}Nb_{0.12}O_x$ catalysts system of dry-, pre-calcined- and calcined samples prepared at various precalcined temperature (448, 498, 548 and 598 K).

It occurs that the same precursor and the same high-temperature calcination give rise to different products highlighting the chemical memory function of the material: a pre-treatment at moderate temperature has a pronounced effect to the formation of a final phase occurring at much higher temperature than the pre-treatment itself. It is clear that the final phase formation does not take place during pre-calcination leaving an almost amorphous intermediate compound with traces of reflections belonging all to the Anderson molybdo-tellurate $TeMo_5O_{16}$ [JCPDS, 1-80-1238].

All the final materials characterized in Figure 4.37 contain the famous five reflections but almost no intensity at the low-angle fingerprint region indicating that the hex phase is the main constituent. The intensity distribution of the survey data indicates, however, that there are variable admixtures of additional Mo-V oxide phases. Amongst them Mo_5O_{14} [JCPDS, 31-1437] and $V_{0.95}Mo_{0.97}$ O5 [JCPDS, 1-77-649] are clearly identified components, others my be present but cannot be identified at this level of pattern quality. Table 4.9 summarizes the crystalline phases of the $Mo_1V_{0.3}Te_{0.23}Nb_{0.12}O_x$ catalyst system at different pre-calcination temperature. None of the samples is similar to the reference mixture shown in Figure 4.33.

b) Effect of Viscosity Enhancer

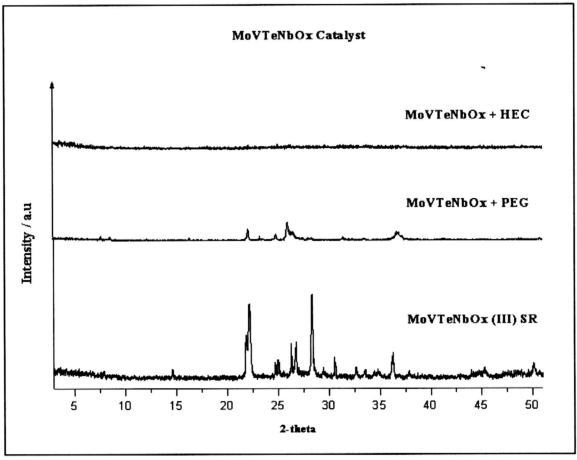

Figure 4.38: X-ray Powder diffraction pattern of $Mo_1V_{0.3}Te_{0.23}Nb_{0.12}O_x$ catalyst system prepared by slurry method with PEG or HEC as a viscosity enhancer.

Figure 4.38 shows the XRD pattern of unpromoted $Mo_1V_{0.3}Te_{0.23}Nb_{0.12}O_x$ catalyst system after adding polyethylene glycol (PEG) or hydroxyl ethyl cellulose (HEC) acting as viscosity enhancers of the preparation solution. Both catalysts were pre-calcined at temperature 548 K and calcined at 873 K under argon for 2 hours. Adding PEG or HEC to the $Mo_1V_{0.3}Te_{0.23}Nb_{0.12}O_x$ catalyst system, resulted in a much more reducing atmosphere during pre-calcination and maybe even during calcination as much of the organic material may have become polymerized into the inorganic solid. Strong supporting evidence for this comes from the morphological characterization discussed in the SEM/EDX section. The reduced calcination temperatures were clearly inappropriate to generate the crystalline mixture characterized by the famous five reflections seen as reference in the lower trace of Figure 4.38. It is evident that none of the phases that should be indicative of good catalytic performance is present in both systems. It remains an open question if the changed calcination conditions or the additional reducing organic additives were responsible for this absence of phase formation.

c) Effect of Precursor

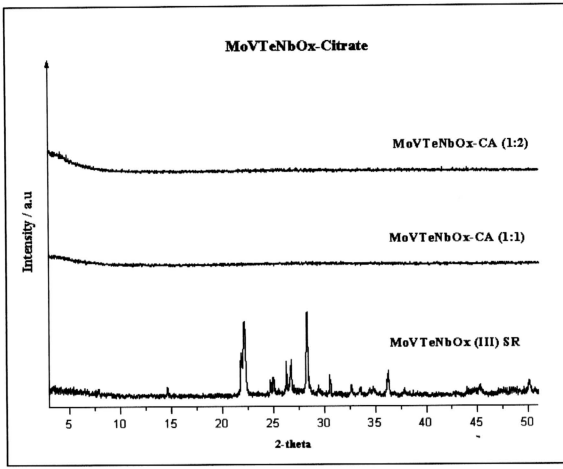

Figure 4.39: X-ray Powder diffraction pattern of $Mo_1V_{0.3}Te_{0.23}Nb_{0.12}O_x$ catalyst system prepared via citric acid route at two ratios- 1:1 & 1:2 metal to citric acid.

Figure 4.39 shows the XRD pattern of $Mo_1V_{0.3}Te_{0.23}Nb_{0.12}O_x$ catalyst system prepared via the citric acid route. This preparation was applied to investigate the effect of complexation of the precursor cations before precipitation. The samples were pre-calcined at 548 K and calcined at 873 K under argon for 2 hours. The XRD pattern show that modification of the $Mo_1V_{0.3}Te_{0.23}Nb_{0.12}O_x$ catalyst system prepared via citric acid route results to a fully X-ray amorphous systems for both abundances of modifier being applied. In comparison to the viscosity enhancer here the standard calcination conditions were applied and still no crystallization can be stated by XRD. This supports the allegation that a too- reducing gas phase during pre-calcination disturbs the metal-

oxygen framework in the intermediate state such that during the main calcination that is executed in the absence of oxygen the deficit in the anion lattice cannot be replenished after the use of structural oxygen for burning organic material. The main calcinations conditions do not allow to replenish the oxygen stoichiometry do not also ensure the complete loss of all organic carbonized residues (see SEM/EDX section) and do not allow to hold the cations of the structure in their appropriate oxidation state to form the desired phases. These oxidation states are for the desired phases close to the highest possible maximum valences. The undesired side phases are more deeply reduced and at the expected substantial loss of oxygen during pre-calcinations the whole system is likely to fall apart into binary sub-oxides such as Mo_4O_{11} and VO_2. There is thus ample reason for the solid to be ill-ordered under inappropriate oxygen partial pressures during phase formation. The data suggest that preparations containing excess amount of organic additives may thus have to be calcined in a different regime of gas composition and maybe using a different temperature-program rather than the materials from the standard recipe. This recipe is much leaner in reducing species during ligand removal and does also not offer the stoichiometry to form a carbon skeleton for a carbon-inorganic composite that easily forms under sub-stoichiometric pre-calcination conditions being very adequate for carbonization of organic matter.

4.4.2 Promoted Mo-V-Te-Nb-Ox $_x$ Catalysts System.

a) Effect of Nickel Promoter

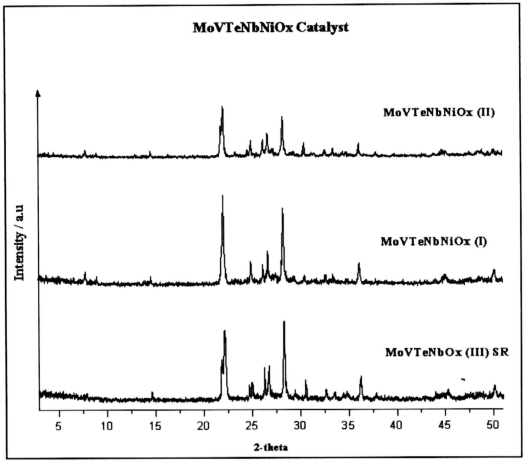

Figure 4.40: X-ray Powder diffraction pattern of $Mo_1V_{0.3}Te_{0.23}Nb_{0.12}NiO_x$ catalyst system prepared by slurry method adding nickel as promoter with two different weight loading 0.05 (MoVTeNbNiOx I) and 0.005 (MoVTeNbNiOx II) atomic percent, compared with standard recipe pattern (MoVTeNbOx III).

Figure 4.40 shows the XRD pattern of promoted $Mo_1V_{0.3}Te_{0.23}Nb_{0.12}NiO_x$ catalyst, to study the effect of nickel addition on the phase evolution of the $Mo_1V_{0.3}Te_{0.23}Nb_{0.12}O_x$ catalyst system. This catalyst was pre-calcined at 548 K and calcined at 873 K under argon for two hours. Both the dried and pre-calcined samples of MoVTeNbNiOx exhibit poorly crystalline phases. The crystallization only occurs after the calcinations process.

The XRD result shows clearly that adding nickel as a promoter affects the crystallinity of the sample. This is unexpected as so little of the material was added that might barely give rise to any discernible diffraction intensity has an effect on the overall structure. This shows that at least one of the prompting functions is that of a structural promoter affecting the phase formation. The observation implies further that within the limits of reproducible diffraction data acquisition the poor quality of the diffraction patterns is not the effect of self-absorption but of on an average poor diffraction power pointing to coherence length problems when taking into account the overall good crystalline morphology seen in the SEM/EDX part. It occurs further that the abundance of the ortho phase in the mixture indicated by the famous five reflections and by the now discernible low-angle reflections has markedly increased in the 0.05% sample. In accordance with the thermal analysis data this observation fits the idea that during calcinations there should be no reducing components in the system: the addition of the transition metal catalyzes the gasification of ligands and thus reduces the abundance of residual species consuming oxygen during the crucial phase formation process in the main calcination reaction. The SEM-micrographs of this catalyst (*Figure 4.27 and 4.28*) shows that at high weight loading segregation of a Ni phase on the crystals of the Anderson phase occurs whereas at low loading no effect on the sample morphology was detected. Table 4.10 summarised the crystalline phase of promoted $Mo_1V_{0.3}Te_{0.23}Nb_{0.12}NiO_x$ catalyst system compared with the standard recipe (MoVTeNbx III catalyst).

b) Effect of Chromium Promoter

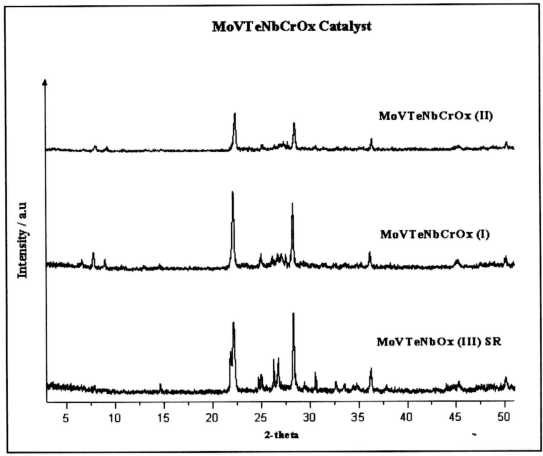

Figure 4.41: X-ray powder diffraction pattern of promoted $Mo_1V_{0.3}Te_{0.23}Nb_{0.12}CrO_x$ catalyst system prepared by slurry method adding chromium as promoter at two different weight loading 0.05 (MoVTeNbCrOx I) and 0.005 (MoVTeNbCrOx II) atomic percent, compared with standard recipe pattern (MoVTeNbOx III).

Figure 4.41 shows the XRD pattern of promoted $Mo_1V_{0.3}Te_{0.23}Nb_{0.12}CrO_x$ catalyst to study the effect of chromium to the $Mo_1V_{0.3}Te_{0.23}Nb_{0.12}O_x$ catalyst system. This catalyst was pre-calcined at 548 K and subsequently calcined at 873 K under argon for 2 hours. Benefiting from the identical calcinations conditions, the effect of the different transition metal additives on the structure-formation processes can be directly compared and related to the structure of the non-promoted system. In agreement with the observation in the Ni system it is evident that Cr addition strongly enhances the abundance of the ortho phase and even when only 0.005% were added.

The fact that a different metal ion is more efficient in modifying the phase formation may be indicative that it is of relevance at which point in thermal pre-history of the sample the detrimental reducing species are removed. Both the temperature level and the local thermal overheating during the catalysed oxidation are different for Ni and Cr. In particular, the effect of a thermal shock during pre-calcination that was clearly evidenced in the TGA experiments and is seen in the TPR data may be of beneficial function in bringing about the ortho phase. This phase is the least stable phase in the phase cocktail of the MoVTe system and either forms with the most demanding kinetics or is most easily destroyed at the high calcinations temperatures used for the phase formation process during the main calcination. The fact that a very crystalline variant of the ortho phase is obtained if no calcination but hydrothermal synthesis is applied [77] underlines this kinetic liability of the target phase.

c) Effect of Cobalt Promoter

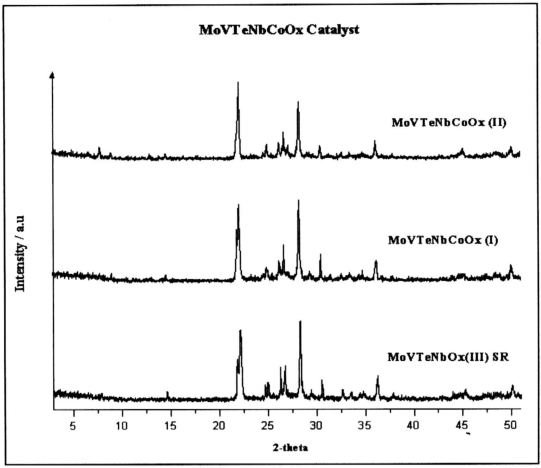

Figure 4.42: X-ray Powder diffraction pattern of promoted $Mo_1V_{0.3}Te_{0.23}Nb_{0.12}$ CoO_x catalyst system prepared by slurry method adding cobalt as a promoter at two different weight loading 0.05 (MoVTeNbCoOx I) and 0.005 (MoVTeNbCoOx II) atomic percent, compared with standard recipe pattern (MoVTeNbOx III).

Figure 4.42 show the XRD pattern of promoted $Mo_1V_{0.3}Te_{0.23}Nb_{0.12}CoO_x$ catalyst system to study the effect of cobalt. These catalysts were pre-calcined at a temperature 548 K and calcined at 873 K under Argon for 2 hours. The XRD patterns show very little differences with respect to that of the reference Sample: Co addition seems not to interfere with the redox chemistry of the ligand removal and hence also not to affect the phase formation process. This observation allows the exclusion on the notion that the function of the transition metal addition could be something different than changing the calcination chemistry; all transition metals would stabilize defects in

a densely packed arrangement of octahedral by either providing tetrahedral linkers (Cr, Ni) or by inducing strain due to different distortion for Mo, V and dopant-containing octahedral. This effect is well-documented in close-packed oxides but plays only a negligible role in the present non-densely packed structures that are tolerant to cation substitution already in the reference system.

In summary, the XRD investigation revealed that all samples contain mainly the hex phase of the target systems with the pentagonal bipyramid motif. The ortho phase is present in some samples as a minority contribution. The literature claim about the assignment of phases using the famous five reflections must be taken with great care as evidenced by the reference preparation.

The phase formation and phase distribution can be affected by changing the redox reactions during pre-calcination and calcination. This indicates the highly metastable character of the catalytically relevant target phases. The admixtures of foreign phase that does not contain the pentagonal bipyramid leads the way to stabilisation of the system. It also appears that the parent phase with the pentagonal bipyramid namely the Mo_5O_{14} phase may be of catalytic relevance. In other catalysts used for oxidation of propene and of acrolein this material is the main catalytic active constituent.

XRD is a suitable method to investigate the phase inventory and potentially to infer the kinetics of its formation. There is still much room for improvement in the phase composition of the catalyst taking the literature data of Grasselli as a lead. The analysis has shown how critical the redox chemistry during calcination affects the final structure and how well the systems remember their thermal pre-history. A working

hypothesis for the mode of operation of transition metal additives has been found based on the assumption of additive structure. Activity relationship is valid stating that the ortho phase is the key factor for good catalytic performance in propane oxidation.

Table 4.9: Summary of $Mo_1V_{0.3}Te_{0.23}Nb_{0.12}O_x$ crystalline phase at different pre-calcination temperature.

Sample	Pre-calcine Temperature (K)	XRD crystalline phases
MoVTeNbOx (I)	448	*M2*; $TeMo_5O_{16}$; $V_{0.95}Mo_{0.97}O_5$, Mo_5O_{14}
MoVTeNbOx (II)	498	*M2*; $TeMo_5O_{16}$; $V_{0.95}Mo_{0.97}O_5$, Mo_5O_{14}
MoVTeNbOx (III)	548	*M2*; $TeMo_5O_{16}$; $V_{0.95}Mo_{0.97}O_5$
MoVTeNbOx (IV)	598	*M2*; $TeMo_5O_{16}$ only and minor components $V_{0.95}Mo_{0.97}O_5$

Table 4.10: Summary of promoted $Mo_1V_{0.3}Te_{0.23}Nb_{0.12}O_x$ crystalline phase at two different weight loading.

Sample	Metal (Atomic weight)	XRD crystalline phases
MoVTeNbNiOx (I)	Ni (0.05)	M2 + $TeMo_5O_{16}$ + $V_{0.95}Mo_{0.97}O_5$
MoVTeNbNiOx (II)	Ni (0.005)	M2 + $TeMo_5O_{16}$ + $V_{0.95}Mo_{0.97}O_5$
MoVTeNbCrOx (I)	Cr (0.05)	M2 + $TeMo_5O_{16}$ + $V_{0.95}Mo_{0.97}O_5$
MoVTeNbCrOx (II)	Cr (0.005)	M2 + $TeMo_5O_{16}$ + $V_{0.95}Mo_{0.97}O_5$
MoVTeNbCoOx (I)	Co (0.05)	M2 + $TeMo_5O_{16}$ + $V_{0.95}Mo_{0.97}O_5$
MoVTeNbCoOx (II)	Co (0.005)	M2 + $TeMo_5O_{16}$ + $V_{0.95}Mo_{0.97}O_5$

4.5 Thermal Behavior

Thermal analysis will be used to identify the sequence of events transforming the precipitate into the active oxide. TGA and DTG allow the identification of the number and types, of reactions involving evaporation of small molecules from removal of ligands and of water from condensation or drying processes. These events will also occur in DSC experiments but in addition, some information is gained about processes that do not lead to weight changes. Crystallisation and re-structuring are such processes in the present context. At high temperatures the experiments may be used to check for volatile components of the oxide system where in particular tellurium oxide and vanadium oxide are candidates, as the final calcination temperatures are close to or even above the melting points of some oxide phases.

The transferability of these results to determine the proper thermal treatment conditions is, however, only of limited relevance as the gas composition in a calcination experiment and in the present studies is not identical. The thermal analytical data were all obtained in nitrogen atmosphere under auto reducing conditions. The calcination is divided in two parts: up to a certain pre-calcination temperature where synthetic air is used followed by a higher calcinations temperature under inert conditions. The necessity to split the calcinations into two regimes that was found in all literature reports on this system is a strong indication that the availability of gas phase oxygen during destruction of the reducible ligands is essential to keep the oxide chemistry intact. The requirement to keep the oxygen apart from the high temperature treatment shows that the desired products are labile with respect to over-oxidation; the desired products are sub-oxides with respect to the maximum valence of all cations

present in the MoVTe system. A phase in which all cations are of their respective highest oxidation states does not either exist or is undesirable for catalytic applications. The heating rate chosen was 5 K min^{-1} slow enough to give room to also slow processes to be completed without much kinetic delay. The line shapes of the derivative techniques should thus be representative of the different kinetic requirement for different processes.

4.5.1 Unpromoted $Mo_1V_{0.3}Te_{0.23}Nb_{0.12}O_x$ Catalysts System.

a) Effect of Precalcination Temperature

Figure 4.43 show the thermal behavior of $Mo_1V_{0.3}Te_{0.23}Nb_{0.12}O_x$ catalysts system, where this result obtains by thermal gravimetric analysis (TGA) and differential scanning calorimetry analysis (DSC) with flow of N_2 gas at 50 mL min^{-1}, dynamically run at heating rate of 5 K min^{-1}. Table 4.11 summarises the data from TGA, DSC and DTG curve for this catalyst system.

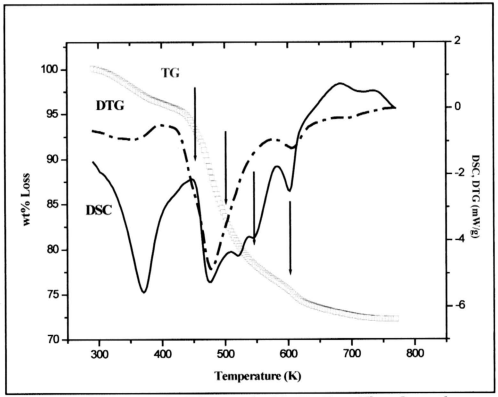

Figure 4.43: TGA, DSC and DTG curve for $Mo_1V_{0.3}Te_{0.23}Nb_{0.12}O_x$ catalyst system.

Figure 4.43: TG, DTG and DSC show the thermogram on standard preparation of MoVTe. The arrows indicate the changeover in temperatures from pre-calcination to calcination that were used during performance optimization.

The pattern in Figure 4.43 shows 4 typical regions:
A low temperature, weight loss occurs with an exothermic net energy change terminated at around 400 K. The main weight change occurs from 450 K to 550 K associated with several processes with an overall surprisingly small exothermic energy balance. This statement is apparently not supported by the data in Table 4.11, which however, becomes clear if one observes that about three times the weight loss occurring in the second phase compared to the first phase creates only a net heat evolution of 30% more than the in first process. A third phase of the complex processes involves only a small weight change up to 613 K and at the final phase of weight loss leads to the overall thermal stability.

The first event is a combination of an endothermic loss of 5.99% water followed by a strongly exothermic polycondensation of the dried solid. This can be concluded from the comparison of the shapes of the DTG and DSC signals indicating the superposition of several consecutive events rather than the execution of a simple drying process that would give rise to a strong DSC signal in the opposite direction. The crystallization occurs further between 400 K and 450 K where without weight loss an exothermic event of re-structuring occurs.

At this stage the solid still contains removable ligands. These ligands are evaporated in a complex multi-step reaction between 440 K and 550 K. The comparison of the DSC and DTG curves allows one to conclude that a preceding step

should be the endothermic polycondensation liberating water followed by the autoxidation of redox-active ligands. This process leading to a weight loss of 17.22 % is overall a highly exothermic process over-compensating the endothermic process of evaporation. Two restructuring events without discernible weight losses follow the removal of the ligands.

The last step of crystallization in phase 4 modifies the solid in a profound way as the heat capacity of the system changes very significantly. Taking into account the nature of the system under study it is concluded that the step at 610 K leads to the formation of an extended solid with a proper densely packed crystal structure whereas the multiple low-temperature events bring about different forms of still supramolecular materials with a poly-ionic crystal structure and small volatile species as counter ions.

Comparison of this analysis with the choice of pre-calcination temperature allows drawing several conclusions. The catalytically successful choice at 548 K is placed at the final phase transformation of the system into a still supramolecular system. It seems disadvantageous to let a system crystallize that is fully coordinated without any inner reactivity of the solid left. It seems also inadequate to keep redox-active ligands during the main calcination and so to support autoreduction. Thus the compromise between preservation of the oxidation state at high temperatures and maintenance of inner solid state reactivity is right at the end of the removal of the redox-active ligands and before the final condensation step of the inorganic solid.

The temporal assignment of the processes and not the attribution of exact temperatures is done deliberately as the detailed inspection of the DTG and DSC curves gives numerous hints about the metastability of the solid state products and hence

towards the inadequacy of phase assignments tacitly done with assigning stability temperatures. This notion is fully in line with the XRD observations of extensive and differing amorphous phases and transient crystallization and re-dissolution of ternary compounds (Andersson phase).

The fact that the optimum pre-calcination temperature in air coincides with a phase-formation event in the thermal analysis done under inert atmosphere points to the redox-labile character of the oxide matrix: the solid is in a position to deliver all oxygen required to remove the ligands present in the standard recipe without being affected in its phase-formation dynamics. The solid acts as a storage medium or sponge for oxygen. This can be seen as an indirect indication of the function of this material as a redox catalyst during which function many moles of oxygen will have to be moved through the gas-solid interface.

a) Effect of Viscosity Enhancer

The $Mo_1V_{0.3}Te_{0.23}Nb_{0.12}O_x$ sample prepared with the addition of PEG or HEC as a viscosity enhancer, cannot be characterized by thermal gravimetry analysis (TGA) and Differential Scanning Calorimetric (DSC) because the samples are still in the gel form after being dried at 353 K. This sample would require a higher drying temperature or the evaporation of the residual water at low pressures (xero-gel or aerogel formation). The observations are in line with XRD data showing that after calcination at temperature 873 K only X-ray amorphous oxides are present. This is further in line with the SEM/EDX data showing the carbon-inorganic oxide of opposite nature and revealing the morphology of a dried gel.

b) Effect of Precursor

For $Mo_1V_{0.3}Te_{0.23}Nb_{0.12}O_x$ prepared via the citric acid route, the sample also cannot be characterized by thermal gravimetry analysis (TGA) and Differential Scanning Calorimetric (DSC), because the sample is still in the gel form after being dried at 353 K. This sample also needs a much higher drying temperature to dry though such procedure may destroy the texture of the catalysts. This result also can be supported by XRD, where after calcination at 873 K, no crystalline peak can be seen. The SEM images reveal flakes-like morphology without a crystalline structure.

4.5.2 Promoted $Mo_1V_{0.3}Te_{0.23}Nb_{0.12}O_x$ Catalysts System.

a) Effect of Promoter

Figures 4.4, 4.45, 4.46, 4.47, 4.48 and 4.49 reveal the thermal behavior of $Mo_1V_{0.3}Te_{0.23}Nb_{0.12}O_x$ catalysts system with the addition of -Ni, -Cr and –Co as a promoter at two different weight loadings. These results were obtained by thermal gravimetric analysis (TGA) and differential scanning calorimetry analysis (DSC) with flow of N_2 gas at 50 mL min^{-1}, dynamically run at 5 K min^{-1} heating rate. Table 4.12, 4.13 and 4.14 summarises the data from TGA, DSC and DTG curves for these catalyst systems. In the following, the promoted systems was analysed in comparison with the standard preparation discussed before. Changes in the thermal behavior was identified without discussing the origin of the four steps that occur in all of these systems.

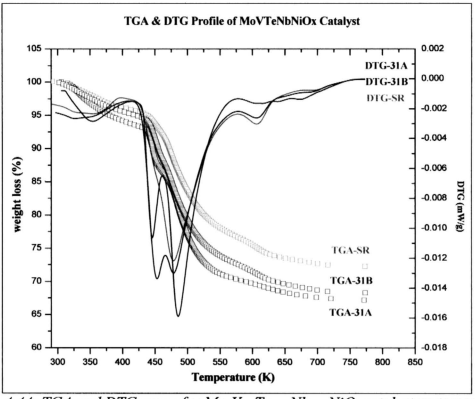

Figure 4.44: TGA and DTG curve for $Mo_1V_{0.3}Te_{0.23}Nb_{0.12}NiO_x$ catalyst system whereas sample number 31A due to MoVTeNbNiOx (I), 31B due to MoVTeNbNiOx (II) and SR represent for standard recipe.

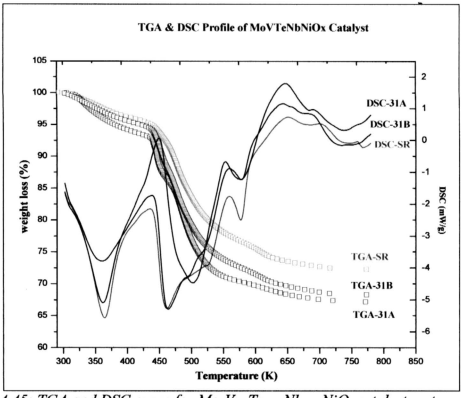

Figure 4.45: TGA and DSC curve for $Mo_1V_{0.3}Te_{0.23}Nb_{0.12}NiO_x$ catalyst system whereas sample number 31A due to MoVTeNbNiOx (I), 31B due to MoVTeNbNiOx (II) and SR represent for standard recipe.

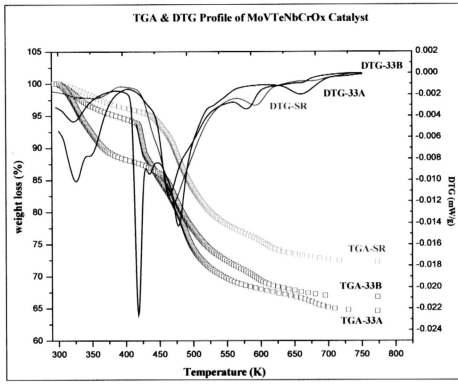

Figure 4.46: TGA and DTG curve for $Mo_1V_{0.3}Te_{0.23}Nb_{0.12}CrO_x$ catalyst system whereas sample number 33A due to MoVTeNbCrOx (I), 33B due to MoVTeNbCrOx (II) and SR represent for standard recipe.

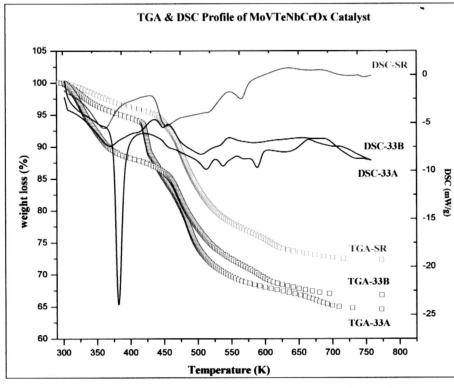

Figure, 4.47: TGA and DSC curve for $Mo_1V_{0.3}Te_{0.23}Nb_{0.12}CrO_x$ catalyst system whereas sample number 33A due to MoVTeNbCrOx (I), 33B due to MoVTeNbCrOx (II) and SR represent for standard recipe.

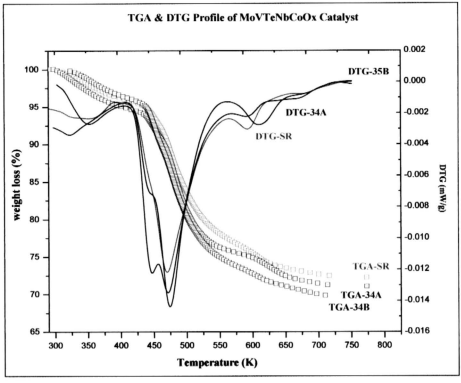

Figure, 4.48: TGA and DTG curve for $Mo_1V_{0.3}Te_{0.23}Nb_{0.12}CoO_x$ catalyst system whereas sample number 34A due to MoVTeNbCoOx (I), 34B due to MoVTeNbCoOx (II) and SR represent for standard recipe.

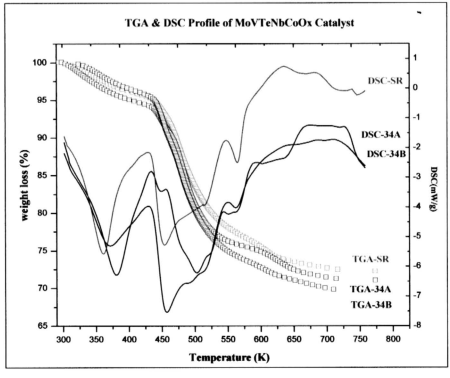

Figure 4.49: TGA and DSC curve for $Mo_1V_{0.3}Te_{0.23}Nb_{0.12}CoO_x$ catalyst system whereas sample number 34A due to MoVTeNbCoOx (I), 34B due to MoVTeNbCoOx (II) and SR represent for standard recipe.

In general, it is most significant that the addition of small amounts of transition metal species affects the thermal behavior of the oxide mixture. This indicates the catalytic operation of the promoter that acts as a structural promoter by changing the redox behavior of the whole metal-ligand system. This conclusion was already reached with the XRD analysis where the addition of these small amounts of promoters changed the overall diffraction pattern without giving rise to additive structural features. The strong and variable structure-directing power of the additives can be judged from the discernible differences by adding less than 1 % of an additional cation to a three-cation system.

Figure 4.44 and 4.45 shows the compilation of data for the Ni system. The top line compares the TG-DTG data and the lower lines compare the TG-DSC traces. It is significant that the total weight loss in the promoted systems is much larger than the addition of cation should give rise to. There is also no proportionality in this additional weight loss. The most likely explanation is the catalytic effect of removing redox-active ligands under auto reducing conditions. This notion is supported by a comparison of the efficiency in structure direction between the three additives using the Figures 4.44, 4.45, 4.46, 4.47, 4.48 and 4.49. Cr is the most redox-active additive and creates the largest additive weight loss whereas Co is the least active one and leads to no significant extra weight loss. This observation fits well with the analysis of the TPR experiments discussed below stating that not all reducible ligand species are removed in the standard preparation even when synthetic air is applied in the pre-calcination step.

The incomplete removal of ligand species that do not belong to an oxide system is a major point when looking for catalyst preparation-activation reproducibility and redox stability of the final catalyst: Only the addition of extra redox cations may lead to a complete removal of the redox-active ligands at temperatures and duration of the pre-calcination before the final condensation process leads to the active oxide mixture.

It is obvious that the mixture of phases may well be controlled by the chemical potential prevailing during the final condensation process. This was also discussed in the XRD section and the present findings support the view that promotion of the genesis of the active phase is an important element in optimization strategies of the MoVTe system.

In the Ni system the addition of the large amount of promoter seriously affects the kinetics of ligand decomposition. The steep changeover in rates at 435 K indicates a kinetically hindered (explosive) decomposition that will affect the microstructure and the crystallization behavior due to creation of local overheating and strong multiple crackling during liberation of volatile ligands. This effect leads also to the pronounced splitting of the main signals in DSC and DTG.

In the Cr system similar effects are found. Here a special observation concerns the efficiency of the promotion; it is very obvious that the less concentrated promoter is much more effective in changing the redox behavior of the ligand system. This is seen as indication about the function of the promoter. Only highly disperse (eventually monomeric) promoter species are effective, particles or clusters of promoter are less suitable or inefficient. Dispersion matters very significantly and so it would be appropriate to minimize the amount of additive. The Cr data also clearly support the

interpretation of the occurrence of several reaction steps during one weight loss episode as stated in the discussion of the data from the standard sample. The displacement of the sharp peaks in DSC and DTG shows that for a highly efficient promotion of ligand removal, the decomposition kinetics becomes faster than the gas transport kinetics allowing separation of the endothermic ligand removal and the exothermic oxidation.

It is apparent that for Ni and Cr the choice of the final pre-calcination temperature is inadequate if the system should be still reactive. The phase formation processes of supramolecular oxides are occurring at lower temperatures due to the catalytic ligand removal and hence the pre-calcination temperatures should be re-adjusted. This will also be found in the TPR data discussed below.

The Co system is the least effective and hence most similar in its behavior to the standard system. At high Co loading a qualitative change of the process profiles indicates again the composite nature of the first and second phases of solid transformation. There seems to be a retarding effect on all redox processes with Co addition. The strong tendency of Co to react with Mo species to form cobalt-molybdates may be an explanation to this observation.

In summary the thermal analysis data clearly reveal the complex interplay of ligand removal, polycondensation and phase formation occurring in several intertwined processes separated by temperature. The separation is affected by the redox chemistry of the system. This redox chemistry can be modified by the addition of redox-active transition metal species. It can be recommended that the addition of a very small amount of Cr to the system and appraisal on the optimal calcination process may well bring about a very different catalyst as the solid state transformations will occur at

lower temperatures and at a more constant chemical potential without residual autoreduction during the main calcination step will not interfere with the formation of the metastable desired phase mixture M1/M2.

The methodology of optimizing the calcination by thermal analysis would be greatly improved if a variable atmosphere could be applied to the system and a non-linear but concentration-driven heating rate would be applied. As these modes of operation will require new instrumentation to be developed, their application goes far beyond the possibilities of work in this thesis. The present work may serve as an incentive to initiate such instrumental developments taking into consideration the enormous amount of time that would be saved in catalyst development when adequate adjustment to the calcination conditions were applied to chemically modify catalyst formulations.

Table 4.11: Summarized data from TGA, DSC and DTG curve for $Mo_1V_{0.3}Te_{0.23}Nb_{0.12}O_x$ catalyst system.

Type of Catalyst	TGA & DTG Analysis Result											
	1st Process		2nd Process		3rd Process		4th Process		5th Process		RESIDUE
	T_{TG} / T_{DTG}	%	T_{TG} / T_{DTG}	%	T_{TG} / T_{DTG}	%	T_{TG} / T_{DTG}	%	T_{TG} / T_{DTG}	%	%
MoVTeNbOx	T_{TG} **303 - 396 K**	3.79	T_{TG} **396 - 445 K**	2.2	T_{TG} **445 - 577 K**	17.46	T_{TG} **577 - 639 K**	2.89	T_{TG} **639 – 761 K**	1.47	72.28
	T_{DTG} **396 K**		T_{DTG} -		T_{DTG} **577 K**		T_{DTG} **639 K**		T_{DTG} -		

Type of Catalyst	Differential Scanning Calorimetry (DSC) Analysis Result											
	1st Transition		2nd Transition		3rd step Transition		4th step Transition		5th step Transition		6th step Transition	
	Peak (K)	ΔH (m/J)	Peak (K)	ΔH (m/J)	Peak (K)	ΔH (m/J)	Peak (K)	ΔH (m/J)	Peak (K)	ΔH (m/J)	Peak (K)	ΔH (m/J)
MoVTeNbOx	370.32	-2361.57 (Exo)	476.42	-3009.64 (Exo)	603.35	-282.21 (Exo)	710.78	-35.34 (Exo)	772.16	-102.53 (Exo)	809.23	-26.08 (Exo)

(T_{TG} = TG temperature, T_{DTG} = DTG temperature)

Table 4.12: Summarized data from TGA, DSC and DTG curve for $Mo_1V_{0.3}Te_{0.23}Nb_{0.12}Ni_{0.05}O_x$ and $Mo_1V_{0.3}Te_{0.23}Nb_{0.12}Ni_{0.005}O_x$ catalyst system.

Type of Catalyst	TGA & DTG Analysis Result										
	1st Process		2nd Process		3rd Process		4th Process		5th Process		RESI-DUE
	T_{TG} / T_{DTG}	%	T_{TG} / T_{DTG}	%	T_{TG} / T_{DTG}	%	T_{TG} / T_{DTG}	%	T_{TG} / T_{DTG}	%	%
MoVTeNb OxNi (I)	T_{TG} **303-415 K** / T_{DTG} **415 K**	3.79	T_{TG} **415–463 K** / T_{DTG} -	4.95	T_{TG} **463– 575 K** / T_{DTG} **575 K**	16.23	T_{TG} **575–656 K** / T_{DTG} -	2.39	T_{TG} **656–767 K** / T_{DTG} **723 K**	1.62	70.62
MoVTeNb OxNi (II)	T_{TG} **303–419 K** / T_{DTG} **419 K**	4.9	T_{TG} **419–465 K** / T_{DTG} **465 K**	7.58	T_{TG} **465– 578 K** / T_{DTG} -	15.01	T_{TG} **578– 642 K** / T_{DTG} **642 K**	2.66	T_{TG} **642–761 K** / T_{DTG} -	1.57	63.31

Type of Catalyst	Differential Scanning Calorimetry (DSC) Analysis Result							
	1st step Transition		2nd step Transition		3rd step Transition		4th step Transition	
	Peak (K)	ΔH (m/J)	Peak (K)	ΔH (m/J)	Peak (K)	ΔH (m/J)	Peak (K)	ΔH (m/J)
MoVTeNbOxNi (I)	369	-3353.63 (Exo)	522.02 ,	-6083.08 (Exo)	713.73	-53.17 (Exo)	776.19	-382.44 (Exo)
MoVTeNbOxNi (II)	366.13	-1891.04 (Exo)	479.17	-3310.71 (Exo)	605.34	-193.04 (Exo)	766.91	-491.16 (Exo)

Table 4.13: Summarized data from TGA, DSC and DTG curve for $Mo_1V_{0.3}Te_{0.23}Nb_{0.12}Cr_{0.05}O_x$ and $Mo_1V_{0.3}Te_{0.23}Nb_{0.12}Cr_{0.005}O_x$ catalyst system.

Type of Catalyst	Thermal Gravimetry Analysis Result												
	1st Process		2nd Process		3rd Process		4th Process		5th Process		6th Process		
	T_{TG} T_{DTG}	%	T_{TG} T_{DTG}	%	T_{TG} T_{DTG}	%	T_{TG} T_{DTG}	%	T_{TG} T_{DTG}	%	T_{TG} T_{DTG}	%	%
MoVTeNb OxCr (I)	T_{TG} **303–399 K**	5.4	T_{TG} **399–439 K**	6.91	T_{TG} **439–457 K**	3.27	T_{TG} **457–532 K**	13.6	T_{TG} **532–641 K**	3.6	T_{TG} **641–731 K**	2.3	64.
	T_{DTG} **399 K**	6	T_{DTG} -		T_{DTG} **532 K**		T_{DTG} -	2	T_{DTG} -	5	T_{DTG} **731 K**		61
MoVTeNb OxCr (I)	T_{TG} **303–345 K**	7.1	T_{TG} **345–409 K**	4.88	T_{TG} **409–451K**	2.02	T_{TG} **451– 99 K**	8.46	T_{TG} **499–573 K**	6.4	T_{TG} **573–710 K**	4.3	66.
	T_{DTG} **409 K**	6	T_{DTG} -		T_{DTG} **573 K**		T_{DTG} -		T_{DTG} **642 K**	5	T_{DTG} -		83

Type of Catalyst	Differential Scanning Calorimetry (DSC) Analysis Result											
	1st step Transition		2nd step Transition		3rd step Transition		4th step Transition		5th step Transition		6th step Transition	
	Peak (K)	ΔH (m/J)	Peak (K)	ΔH (m/J)	Peak (K)	ΔH (m/J)	Peak (^{O}C)	ΔH (m/J)	Peak (K)	ΔH (m/J)	Peak (K)	ΔH (m/J)
MoVTeNb OxCr (I)	379.14	-2930.82 (Exo)	469.56	-61.43 (Exo)	532.54	-1758.45 (Exo)	623.72	-385.48 (Exo)	726.87	-9.72 (Exo)	788.88	-174 (Exo)
MoVTeNb OxCr (I)	394.43	-3167.16 (Exo)	542.44	-430.84 (Exo)	572.10	-152.08 (Exo)	630.37	-196.23 (Exo)	685.71	-341.35 (Exo)	752.64	-72.06 (Exo)

Table 4.14: Summarized data from TGA, DSC and DTG curve for $Mo_1V_{0.3}Te_{0.23}Nb_{0.12}Co_{0.05}O_x$ and $Mo_1V_{0.3}Te_{0.23}Nb_{0.12}Co_{0.005}O_x$ catalyst system.

Type of Catalyst	TGA & DTG Analysis Result										
	1st Process		2nd Process		3rd Process		4th Process		5th Process		RESI -DUE
	T_{TG} / T_{DTG}	%	T_{TG} / T_{DTG}	%	T_{TG} / T_{DTG}	%	T_{TG} / T_{DTG}	%	T_{TG} / T_{DTG}	%	%
MoVTeNb OxCo (I)	T_{TG} **303–415 K** / T_{DTG} **415 K**	5.4	T_{TG} **415 –459 K** / T_{DTG} -	3.51	T_{TG} **459–573 K** / T_{DTG} **486 K**	15.55	T_{TG} **573 – 672 K** / T_{DTG} -	3.7	T_{TG} **672 – 745 K** / T_{DTG} -	0.82	71.08
MoVTeNb OxCo (II)	T_{TG} **303– 417 K** / T_{DTG} **402 K**	3.96	T_{TG} **417 – 467 K** / T_{DTG} -	6.9	T_{TG} **467– 579 K** / T_{DTG} **503 K**	15.51	T_{TG} **579 – 641 K** / T_{DTG} -	2.32	T_{TG} **641 – 758 K** / T_{DTG} -	1.69	69.66

Type of Catalyst	Differential Scanning Calorimetry (DSC) Analysis Result							
	1st step Transition		2nd step Transition		3rd step Transition		4th step Transition	
	Peak (K)	ΔH (m/J)	Peak (K)	ΔH (m/J)	Peak (K)	ΔH (m/J)	Peak (K)	ΔH (m/J)
MoVTeNbOxCo (I)	392.53	-2997.50 (Exo)	530.34	-1979.85 (Exo)	603.76	-231.30 (Exo)	686.10	-321.90 (Exo)
MoVTeNbOxCo (II)	379.57	-1546.64 (Exo)	479.64	-3276.51 (Exo)	603.01	-88.45 (Exo)	703.96	-11.23 (Exo)

4.6 Reduction behavior

Temperature programmed reduction (TPR) was used to evaluate the effect of compositional variation of MoVTe on the propensity towards chemical reduction. Under catalysis conditions the mixed oxide must be present in a partly reduced state to be able to activate oxygen. On the other hand the partial pressure of organic molecules and the chemisorbed hydrogen from C-H activation must not reduce the mixed oxide into a mixed metal state. The resolution of the reduction process in temperature allows further evaluation on the integrity of the samples in terms of phase uniformity. Possible surface reactions of the "lattice oxygen" suspected to be relevant for catalysis were not targeted by the present study, which focused on the bulk behavior.

4.6.1 Unpromoted $Mo_1V_{0.3}Te_{0.23}Nb_{0.12}O_x$ Catalysts System.

a) Effect of Precalcination Temperature

Figure 4.50 show the extent of oxygen removal from several unpromoted $Mo_1V_{0.3}Te_{0.23}Nb_{0.12}O_x$ catalysts precalcined at different temperatures. The measurements were carried out by temperature-programmed reduction in a flow of dilute H_2 gas (5% H_2 in N_2) 25 mL min^{-1}. Table 4.15 show the data summarized from the TPR profile. Crude information about the apparent activation energy can be estimated from the TPR profile for the $Mo_1V_{0.3}Te_{0.23}Nb_{0.12}O_x$ catalyst. The value of activation energy is calculated from a modified Redhead equation [83] as follows:

$$\frac{E_r}{RT_m^2} = \left(\frac{A_r}{\beta}\right)[H_2]_m \exp\left(\frac{-E_r}{RT_m}\right) \qquad (4.6)$$

where E_r is the reduction activation energy (kJ mol^{-1}), T_m is the peak maximum temperature (K) in the rate of the H_2 consumption, A_r as a reduction pre-exponential term (cm^3 $mol^{-1}s^{-1}$) with standard collision number of 10^{13} cm^3 $mol^{-1}s^{-1}$ and $[H_2]_m$ is the gas phase concentration of hydrogen (mol cm^{-3}) at the peak maximum. The values of reduction activation energy of $Mo_1V_{0.3}Te_{0.23}Nb_{0.12}O_x$ catalyst system are summarized in Table 4.15. It must be pointed out that these data are crude estimates, as the assumptions that allow deriving the Redhead formula are certainly not fulfilled for such complex bulk-gas phase reactions. As a means to compare kinetic parameters of a set of similar processes in similar compounds the data are useful even when their numerical values may be significantly erroneous.

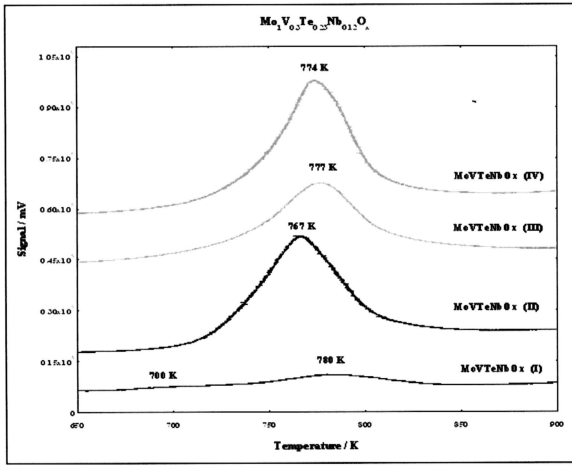

Figure 4.50: TPR profiles of unpromoted $Mo_1V_{0.3}Te_{0.23}Nb_{0.12}O_x$ catalysts system at various precalcination temperatures.

The TPR profiles reveal that the same precursor leads to 4 totally different materials depending on the precalcination temperature. This can be rationalised when the analysis is done using the TG-DSC data. The precalcination temperatures of the present samples are indicated in Figure 4.50. It occurs that the two lower temperatures were chosen below and during the main decomposition step of the volatile components of the precursor. The third temperature is associated with a restructuring of the precursor whereas the highest temperature coincides with the final loss of volatiles (oxygen) from the precursor.

Figure 4.50 reveals that the reduction in all cases sets in at about the operation temperatures of the catalyst namely around 673 K. Peak temperatures and the kinetics of the processes as reflected by the line profiles are different in all four cases. This is a clear indication that the reductive stability and the phase inventory depend on the precalcination temperature and hence "remember" the gas-solid reactions described with the TG-DSC experiments. It is also evident that despite the common precursor the precalcination process renders them all different materials with the same chemical composition. For a homogeneous oxide of a polyvalent metal cation it may be expected to observe a multiple reduction profile with a pre-peak and a main peak indicating the formation of an intermediate compound (sub-oxide). At the low heating rate applied one may also expect to see an induction period after nucleation of the intermediate phase. All this could explain a sloping profile at low temperatures with acceleration towards the peak reduction rate. The multiple profiles in the Figure and the pronounced changes of this profile with pre-treatment temperature exclude this interpretation: It has to be assumed that a mixture of components (eventually phases) is present and that the composition of this mixture depends in spite of the common precursor on the thermal pre-history. The data in Table 4.15 indicates that the chemical potential of the dilute

hydrogen and/or the removal of the water product were insufficient to achieve complete reduction to the metal.

The percentage of oxygen removed is a hypothetical number as the exact content of oxygen was not known. The data refer to a nominal composition based upon the assumption of a highly oxidised starting material. This assumption is justified by the colour of the material indicating the presence of all cations in their highest oxidation states.

The lowest precalcination temperature did not remove the structural water. It allows hence the material to be in a stable form and being resistant to chemical reduction. This is of importance with respect to a possible explanation on the role of steam addition under reaction condition: if the oxide can be kept in a partly hydrated form it will remain in a high overall oxidation state even under the presence of a strongly reducing atmosphere. The lower formal activation energy and the small amount of about 1% total oxygen removed at the pre-peak at 700 K allow to assign this feature to a surface-reduction of the overall still highly oxidised system. This feature will be hidden under the reduction profiles of the stronger precalcined samples.

The sample calcined at 498 K still contains volatiles that are released under reducing conditions. This explains the low peak temperature and the high apparent degree of reduction.

The low high-temperature samples give a more genuine picture of the reactivity of the system. The facts that phase transitions are still occurring (DSC) explains the differing peak profiles reflecting different compositions of the mixture. Each

component exhibits a characteristic reductive stability adding up to a "spectrum" of reduction behaviour reflected in the Figure 4.50. For this reason it is not adequate to further analyse the data in terms of a kinetic model as no indication about the complete phase content is available as also indicated by the featureless XRD profiles of Figure 4.37. The sample precalcined at 548 K is the most genuine "homogeneous" material as indicated by the highest peak reduction temperature. Its profile is contained as key component in the profile of the 598 K sample that is dominated, however, by the reduction profile of a less stable species having occurred from the final weight loss and phase transition at this temperature.

From these data it is adequate to fix the precalcination temperature to 548 K as this is the best compromise between removal of volatile components of the precursor and destruction of the phase inventory of "precalcined MoVTe" which still is not a homogeneous material and a single phase as can be seen from the by far too symmetrical reduction profile. The superficial assumption that precalcination at 498 K should be more adequate as then the highest yield of labile oxygen would be available for selective oxidation ("lattice oxygen" hypothesis) is incorrect as this material is still not fully precalcined in the sense that all volatiles from the precursor synthesis are removed. This is strongly supported by the evolution of the BET surface area showing its maximum at 548 K where all crystallites of the precursor have fallen apart due to the gas evolution and initial reduction. At higher temperatures phase segregation and hence sintering of the most active state have occurred reducing both surface area and most likely also the specific catalytic performance.

Table 4.15: Data summarized from TPR profile of $Mo_1V_{0.3}Te_{0.23}Nb_{0.12}O_x$ catalyst system.

Type of Catalysts	Reduction activation energy, E_r kJ mol^{-1}	T_{max} / K	Total amount O_2 removed (mol $gram^{-1}$)	Total amoun O_2 removed atom $gram^{-1}$	Percentage of oxygen removed / %
MoVTeNbOx (I)	130.5	700	2.1×10^{-4}	1.3×10^{20}	8.06
	145.4	780	1.0×10^{-3}	6.0×10^{20}	
Total oxygen removed:			1.2×10^{-3}	**7.3×10^{20}**	
MoVTeNbOx (II)	142.9	767	5.2×10^{-3}	**3.1×10^{21}**	34.6
MoVTeNbOx (III)	145.6	777	**4.3×10^{-3}**	**2.6×10^{21}**	28.6
MoVTeNbOx (IV)	144	774	4.3×10^{-3}	**2.6×10^{21}**	28.6

- Surface area: MoVTeNbOx (I) = 2.33 $m^2 g^{-1}$
  MoVTeNbOx (II) = 2.73 $m^2 g^{-1}$
  MoVTeNbOx (III) = 10.5 $m^2 g^{-1}$
  MoVTeNbOx (IV) = 5.37 $m^2 g^{-1}$

- Percentage of oxygen removed (%) =

$$\frac{\text{Total amount of oxygen removed (mol } g^{-1})}{\text{Total amount oxygen of } Mo_1V_{0.3}Te_{0.23}Nb_{0.12}O_x \text{ (mol } g^{-1})} \times 100\%$$

b) Effect of Viscosity Enhancer

Figure 4.51 shows the reduction behavior of unpromoted $Mo_1V_{0.3}Te_{0.23}Nb_{0.12}O_x$ catalyst system with adding PEG or HEC as a viscosity enhancer. Table 4.16 summarizes the numerical data from these TPR profiles.

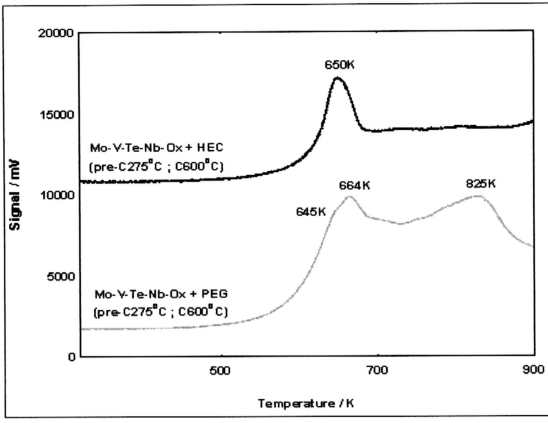

Figure 4.51: TPR result for unpromoted $Mo_1V_{0.3}Te_{0.23}Nb_{0.12}O_x$ catalysts system adding PEG or HEC as a viscosity enhancer.

From the TPR profiles it is clear that adding PEG or HEC as a viscosity enhancer to $Mo_1V_{0.3}Te_{0.23}Nb_{0.12}O_x$ catalysts system changes the morphology and structure of the active $Mo_1V_{0.3}Te_{0.23}Nb_{0.12}O_x$ catalysts system. The TPR profile $Mo_1V_{0.3}Te_{0.23}Nb_{0.12}O_x$ catalysts system with added PEG reveals three reduction peaks where the maximum reduction peaks are at 645 K, 664 K and 825 K. The amount of total oxygen removed from this catalyst is 2.69 x 10^{21} atom $gram^{-1}$. Different with PEG, HEC gives only one single reduction peak at temperature 650 K and the total oxygen removed from the catalyst is only 5.6 x 10^{20} atom $gram^{-1}$, respectively.

Table 4.16: Data summarized from TPR profile of $Mo_1V_{0.3}Te_{0.23}Nb_{0.12}O_x$ adding PEG or HEC as a viscosity enhancer.

Type of Catalysts	Reduction activation energy, E_r kJ mol^{-1}	T_{max} / K	Total amount O_2 removed (mol $gram^{-1}$)	Total amount O_2 removed (atom $gram^{-1}$)	Percentage of oxygen removed / %
	120	645	8.5×10^{-4}	**5.1×10^{20}**	
MoVTeNbOx +	124	664	7.1×10^{-4}	**4.2×10^{20}**	29.7
PEG	154	825	2.9×10^{-3}	**1.7×10^{21}**	
Total oxygen removed:			4.46×10^{-3}	**2.69×10^{21}**	
MoVTeNbOx + HEC	121	650	9.3×10^{-4}	**5.6×10^{20}**	6.2

- Surface area: MoVTeNbOx + PEG = $6.73 m^2 g^{-1}$
  MoVTeNbOx + HEC = $5.5 m^2 g^{-1}$

- Percentage of oxygen removed (%) =

$$\frac{\text{Total amount of oxygen removed (mol } g^{-1})}{\text{Total amount oxygen of } Mo_1V_{0.3}Te_{0.23}Nb_{0.12}O_x \text{(mol } g^{-1})} \times 100\%$$

It is evident that these systems are unsuitable as catalysts as their bulk reduction would be ongoing under operation conditions of 673 K. The adverse effect of excessive organic additives is very clearly demonstrated preventing the formation of a stable phase inventory during precalcination as severe lowering of the oxygen partial pressure during crystallisation resulted in only amorphous materials. It is not surprising that the different stability and reduction power of the two additives lead to two different mixtures of materials. The analytical power of TPR is demonstrated to detect this structural difference in a material that is identically X-ray amorphous. The multiple and different peak structures of these profiles in combination with the profiles of the unmodified materials highlight the enormous potential of the complex composition of the precursor to form and express phases and metastable mixtures under different conditions. These data highlight that there is still much room for optimisation amongst the thermal treatment conditions. As even the XRD with its mixtures of M1 and M2

phase give no clear lead to the best possible catalyst under reduced abundances of steam it is highly desirable to remove all reductive species at the lowest temperature possible and to provide sufficient oxygen partial pressure in the phase formation process at around 548 K to arrive at optimal stable systems. It is significant that the reduction profiles of the two modified samples start at this temperature. The peak profile of the reduction component at about 650 K is indicative of the decomposition of a single phase. The resulting product acts a s catalyst for the deep decomposition of the rest of the material in a very diffuse and unresolved process indicating that its kinetic hindrance e.g. by diffusion out of the inner part of the compact solid is rate-limiting at the heating rate applied. The superimposed peak at higher temperature allows one to conclude that the material from which this feature arises is geometrically not intermixed with the main phase. This is consistent with the multiple morphologies seen in the respective SEM images.

C) Effect of Precursor

Figure 4.52 and Table 4.17 reveal the effects of the presence of citric acid in two concentrations on the reductive stability of samples for unpromoted $Mo_1V_{0.3}Te_{0.23}Nb_{0.12}O_x$ catalysts. Table 4.17 shows the related data.

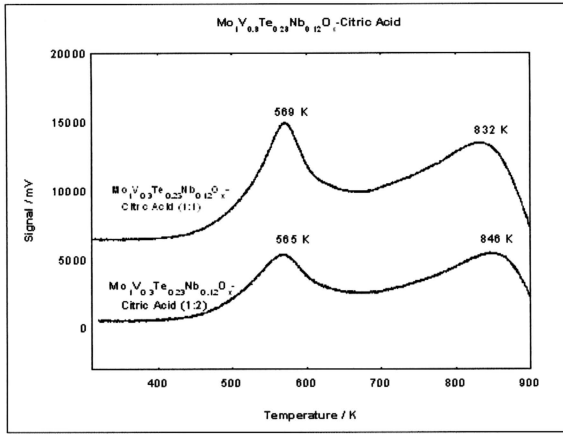

Figure 4.52: TPR result for unpromoted $Mo_1V_{0.3}Te_{0.23}Nb_{0.12}O_x$ catalysts system prepared via citric acid route.

Also these catalysts are inherently unstable under operation conditions. The strongly complexing action of citric acid forming with lower valent cations mononuclear 1:2 complexes and the multi-step decomposition pattern lead to the formation of a nanostructured very reactive oxide form being reduced at 565 K. The fact that this species is twice as abundant with twice the amount of citric acid used strongly supports this assignment. It means that it not possible to infer that this oxide is of different composition than the main material as the expected nanostructuring exerts a strong influence on the reduction kinetics that may well exceed the effect of a different cationic composition. The fact that both samples exhibit no porosity and very compact in their morphology imply that during the precalcination step high temperatures must have been present leading to sintering and even to the decomposition of the oxide structure. The sintered morphology causes then the strong transport limitation of the

reduction-giving rise to the triangular rather than peak shape of the main reduction process.

Nevertheless our speculate that the mixture of materials giving rise to a very broad signal peaking at around 832 K is chemically not identical to the redox-labile material. This is supported by the grossly different apparent activation energy values found in Table 4.52. The phase separation suggested from these profiles is similar to that seen with the viscosity modifiers. In both cases a strong reduction of oxygen available during crystallization of the material will interfere with the generation of a phase with highly oxidized cations. The fact that all precursors were X-ray amorphous supports the notion that a phase separation at the nanoscale may have occurred and that consequently a molybdenum-rich species gives rise to the early reduction peak and a more Nb-rich phase to the high-temperature feature.

Table 4.17: Data summarized from TPR profiles of $Mo_1V_{0.3}Te_{0.23}Nb_{0.12}O_x$ prepared via citric acid route.

Type of Catalysts	**Reduction activation energy, E_r kJ mol^{-1}**	**T_{max} K**	**Total amount O_2 removed (mol gram^{-1})**	**Total amount O_2 removed (atom gram^{-1})**	**Percentage of oxygen removed / %**
MoVTeNbOx (1:1)	107	569	2.7×10^{-3}	**1.6×10^{21}**	42
	156	832	3.6×10^{-3}	**2.2×10^{21}**	
Total oxygen removed:			6.3×10^{-3}	**3.8×10^{21}**	
MoVTeNbOx (1:2)	106	565	2.4×10^{-3}	1.5×10^{21}	34
	159	846	2.7×10^{-3}	1.6×10^{21}	
Total oxygen removed:			5.1×10^{-3}	3.1×10^{21}	

- Surface area: MoVTeNbOx (1:1) = 0.79 $m^2 g^{-1}$
  MoVTeNbOx (1:2) = 0.80 $m^2 g^{-1}$

- Percentage of oxygen removed (%) =

$$\frac{\text{Total amount of oxygen removed (mol g}^{-1})}{\text{Total amount of oxygen of } Mo_1V_{0.3}Te_{0.23}Nb_{0.12}O_x \text{(mol g}^{-1})} \times 100\%$$

4.6.2 Promoted $Mo_1V_{0.3}Te_{0.23}Nb_{0.12}MeO_x$ Catalysts System

a) Effect of Promoter

Figure 4.53, 4.54 and 4.55 show the oxygen consumption for promoted $Mo_1V_{0.3}Te_{0.23}Nb_{0.12}NiO_x$, $Mo_1V_{0.3}Te_{0.23}Nb_{0.12}CrO_x$ and $Mo_1V_{0.3}Te_{0.23}Nb_{0.12}CoO_x$ catalysts with two different compositions of 0.05 and 0.005 atomic units each. Table 4.18 shows the data summarized from the TPR profiles.

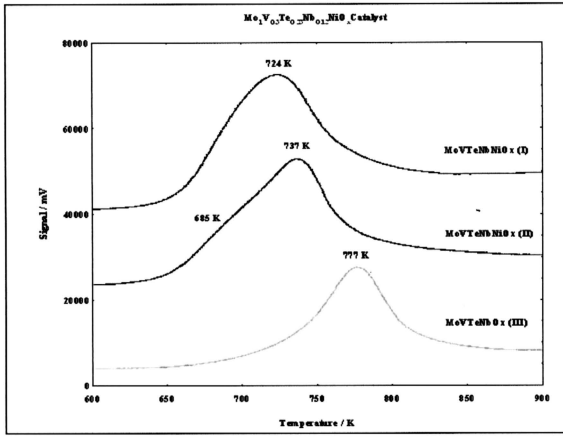

Figure 4.53: TPR result for promoted $Mo_1V_{0.3}Te_{0.23}Nb_{0.12}NiO_x$ catalysts system. Sample III is the unpromoted reference system precalcined as all samples at 548 K. (II is 0.005 % loading and I 0.05 %).

It can be expected from the effects that the promoters had on the precalcination behavior that also the reduction behavior should be different with respect to the unpromoted sample. The lower temperatures at which the main ligand removal occurs

under the catalytic influence of the promoter leaves a different gas composition at 548 K where the phase formation of the second oxide precursor forms from which the final calcinations step starts. This should be reflected by the reducibility. Another influence is the dissolution of at least some of the cations into the molybdate matrix of the MoVTe system that also should affect the reducibility. With 0.05% promotion this should happen to a large extent whereas at 0.5% the formation of a promoter phase may occur. From the chemistry of the promoters it may be expected that Ni and Cr may more strongly act as a co-catalyst for the ligand removal whereas Co is known to form molybdates.

The Ni promoted catalysts is inherently unstable under operating conditions. It is remarkable how non-additive with the presence of 0.005% Ni enhances the reducibility. This can only be the consequence of a profound change in the mixture of the main components brought about in the precalcination or calcinations steps. At higher loading the double-feature structure seems less-well resolved which is likely due to the differing contributions of the two profiles to the overall peak. The occurrence of a difficult-to reduce additional phase with respect to the unpromoted system becomes evident from the baseline drift in the three curves. In agreement with the higher weight loss the presence of the promoters seems to have destabilized the system despite the lower temperature at which the ligand reduction was terminated. This may be seen as clear sign that the Ni got incorporated into the oxide and led to a destabilization and partial phase separation of the system. None of the structures may be assigned to a binary Ni oxide, which would be below the detection limit of the profile (approx. 1% of the total intensity).

For the Cr system the effects are similar in trend with a reduction of the reductive stability but different in detail. The Cr addition causes a splitting of the profile in a high and low-temperature feature from which the low temperature feature is growing with higher loading. At high loading there is a third even less stable component appearing. It is evident again that the promoter affects the solid state chemistry of the whole system and is not a mere additive to the complex mixture of the V-containing matrix material.

The fact that all promoted samples exhibit significant surface areas indicates that all promoter species seem to stabilize small crystallites and prevent sintering at the main calcinations temperature. We expect the promoters to act as linkers between supramolecular clusters and so to stabilize a non-dense ("defective") nanostructure making it more difficult for Ostwald ripening to occur at temperatures below the breakdown of the oxygen sublattice.

In the Co case, the addition of small amounts of promoter has no discernible effect on the redox stability whereas 0.5% addition give rise to a stabilization of the main matrix probably by the formation of Co-molybdates acting again as linkers in the supramolecular structure of the system and hence preventing the initial reduction. The steeper low-temperature tail may be taken as indication for this function.

The data in Table 4.18 show that the addition of each promoter increased the reducibility significantly as much as the amount of oxygen removed is concerned (compare with Table 4.6.1). The chemical memory of the system is shown again as the differences picked up in the precalcination reflect themselves in the reductive stability. Most samples become inherently unstable towards reduction under operation conditions

and it may thus be expected that despite the more labile oxygen lattice which may be positive for "lattice oxygen" to be available, that the structural stability will limit the performance of the promoted systems.

It may be concluded that the addition of the promoters profoundly affected the redox properties of the systems. This must have been achieved through alteration of the main structural features giving rise to the allegation that most of the promoter became dissolved in the main matrix. To exploit this reactivity it would be highly desirable to modify the calcinations procedure such as to try to obtain a crystalline precursor after the precalcination.

From the TPR profile of promoted $Mo_1V_{0.3}Te_{0.23}Nb_{0.12}NiO_x$ catalyst system with nickel as a promoter gives a single reduction peak. This profile show when the weight loading of nickel ~0.005 gives a single peak reduction with a small lump at the temperature 685 K and the maximum reduction temperature are at 737 K. The total oxygen removed from the catalyst surface is 4.5 x 10^{21} atom $gram^{-1}$, which is around 49.3% of oxygen was removed from the catalyst surface, respectively. But when the weight loading of nickel promoter increased to ~0.05 the reduction peak shifted to low temperature and only one maximum reduction temperature can see at 724 K with the total oxygen removed is 4.1 x 10^{-1} atom $gram^{-1}$ where around 45.3% of oxygen was removed. From the TPR result, it is clearly shown that $Mo_1V_{0.3}Te_{0.23}Nb_{0.12}$ NiO_x catalyst with low nickel promoter weight loading (0.005 atomic %) gives a better catalytic activity performance compared then high nickel promoter weight loading (0.05 atomic %) respectively. This reduction activation energy can be calculated with the Redhead equation as follow and applied to the unpromoted and promoted $Mo_1V_{0.3}Te_{0.23}Nb_{0.12}O_x$ catalysts system:

$$\frac{E_r}{RT_{m^2}} = \left(\frac{A_r}{ß}\right)[H_2]_m \exp\left(\frac{-E_r}{RT_m}\right) \qquad (4.6)$$

where E_r is the reduction activation energy (kJ mol^{-1}), T_m is the peak maximum temperature (K) in the rate of the consumption of H_2, A_r as a reduction pre-exponential term ($cm^3mol^{-1}s^{-1}$) which is given the value of a standard collision number of 10^{13} cm^3 mol^{-1} s^{-1} and $[H_2]_m$ is the gas phase concentration of hydrogen (mol cm^{-3}) at the peak maximum. The reduction activation energy for $Mo_1V_{0.3}Te_{0.23}Nb_{0.12}NiO_x$ catalyst with weight loading 0.05 are around 135 kJ mol^{-1} and for 0.005 weight loading are 128.5 kJ mol^{-1} at temperature 685 K and 137.3 kJ mol^{-1} at temperature 737 K *(See the summarized TPR data in table 4.18).*

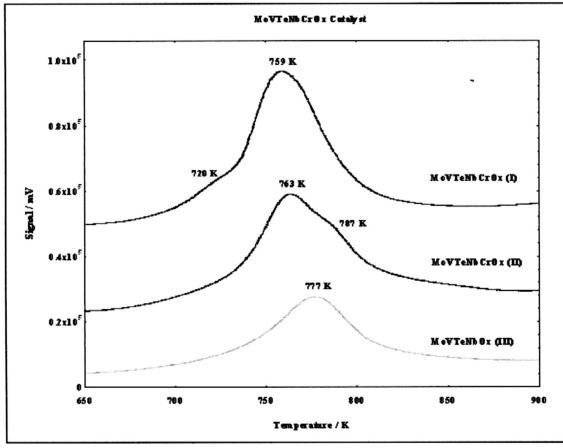

Figure 4.54: TPR result for promoted $Mo_1V_{0.3}Te_{0.23}Nb_{0.12}CrO_x$ catalysts system (I 0.05%, II 0.005 %, III reference).

From the TPR profile of promoted $Mo_1V_{0.3}Te_{0.23}Nb_{0.12}CrO_x$ system catalysts with chromium as a promoted also presents a single sharp peak with a small lump. When the $Mo_1V_{0.3}Te_{0.23}Nb_{0.12}CrO_x$ catalysts with low promoter weight loading (0.005 atomic %) the TPR profile gives single reduction peak at maximum temperature 763 K with a small lump, but when the weight loading increase to 0.05 atomic percent maximum reduction temperature shifted to lower temperature at 759 K and the small lump at 720 K. Total oxygen removed for $Mo_1V_{0.3}Te_{0.23}Nb_{0.12}CrO_x$ catalyst with low promoter weight loading (0.005 atomic %) are almost 4.2 x 10^{21} atom $gram^{-1}$ which is 46.7% of oxygen removed from the surface and for the $Mo_1V_{0.3}Te_{0.23}Nb_{0.12}CrO_x$ catalyst with high promoter weight loading (0.05 atomic %) the total oxygen removed is almost 4.5 x 10^{21} atom $gram^{-1}$ which is around 49.3% of oxygen was removed from the catalyst surface, respectively. From the TPR result, $Mo_1V_{0.3}Te_{0.23}Nb_{0.12}CrO_x$ catalyst system with high chromium weight loading (0.05 atomic %) gives a better catalytic activity performance where this catalyst gives a higher oxygen removed from the catalyst surface which is, this lattice oxygen can assumed as selectivity for the selective oxidation process.

The reduction activation energy for promoted $Mo_1V_{0.3}Te_{0.23}Nb_{0.12}CrO_x$ system can be calculated with the Redhead equation as follow and applied to the unpromoted and promoted $Mo_1V_{0.3}Te_{0.23}Nb_{0.12}O_x$ catalysts system. The value of reduction activation energy for $Mo_1V_{0.3}Te_{0.23}Nb_{0.12}CrO_x$ with low weight loading (0.005 atomic %) is 142.2 $kJmol^{-1}$ at temperature 759 K and for high promoter weight loading (0.05 atomic %) is 141.4 $kJmol^{-1}$ respectively *(See the summarized TPR data in table 4.18).*

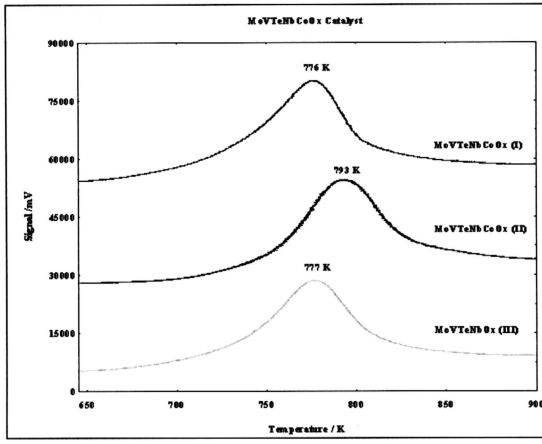

Figure 4.55: TPR result for promoted $Mo_1V_{0.3}Te_{0.23}Nb_{0.12}CoO_x$ catalysts system. (Sample I 0.005%, sample II 0.05 %, sample III reference)

From the TPR profile, promoter $Mo_1V_{0.3}Te_{0.23}Nb_{0.12}CoO_x$ catalysts system shows only one single sharp peak. The $Mo_1V_{0.3}Te_{0.23}Nb_{0.12}CoO_x$ catalysts with low promoter weight loading (0.005 atomic %) gives a value of total oxygen removed is almost 3.1 x 10^{21} atom $gram^{-1}$ at the maximum reduction temperature 793 K. But for $Mo_1V_{0.3}Te_{0.23}Nb_{0.12}CoO_x$ catalyst with high promoter weight loading the maximum reduction temperature was shifted to low temperature at 776 K and gives total oxygen removed is 3.2 x 10^{21} atom $gram^{-1}$, respectively. From this result, it can be concluded that $Mo_1V_{0.3}Te_{0.23}Nb_{0.12}CoO_x$ catalysts with a high promoter weight loading give a better catalytic activity performance with 35.3% total oxygen removed from the catalyst surface compared to low promoter weight loading that only 34% total oxygen was removed.

The reduction activation energy also can be calculated from Redhead equation. The total reduction activation energy for $Mo_1V_{0.3}Te_{0.23}Nb_{0.12}CoO_x$ catalyst with low promoter weight loading is 147.8 $kJmol^{-1}$and for high promoter weight loading is 144.6 $kJmol^{-1}$ respectively. *(See the TPR summarized data from table 4.18).*

Table 4.18: Data summarized from TPR profiles of promoted $Mo_1V_{0.3}Te_{0.23}Nb_{0.12}O_x$ system.

Type of Catalysts	Reduction activation energy, E_t kJ mol^{-1}	T_{max} / K	Total amoun O_2 removed (mol $gram^{-1}$)	Total amount O_2 removed (atom $gram^{-1}$)	Percentage of oxygen removed / %
MoVTeNbNiOx (I)	135.0	724	6.8×10^{-3}	4.1×10^{21}	45.3
MoVTeNbNiOx (II)	128.5	685	1.7×10^{-3}	1.0×10^{21}	49.3
	137.3	737	5.7×10^{-3}	3.4×10^{21}	
Total oxygen removed:			7.4×10^{-3}	4.5×10^{21}	
MoVTeNbCrOx (I)	135.2	720	1.2×10^{-3}	7.2×10^{20}	49.3
	141.4	759	6.2×10^{-3}	3.7×10^{21}	
Total oxygen removed:			7.4×10^{-3}	4.5×10^{21}	
MoVTeNbCrOx (II)	142.2	763	3.6×10^{-3}	2.2×10^{21}	46.7
	147	786	3.4×10^{-3}	2.1×10^{21}	
Total oxygen removed:			7.0×10^{-3}	4.2×10^{21}	
MoVTeNbCOOx (I)	144.6	776	5.3×10^{-3}	3.2×10^{21}	35.3
MoVTeNbCoOx (II)	147.8	793	5.1×10^{-3}	3.1×10^{21}	34

- Surface area: MoVTeNbNiOx (I) = 10.61 $m^2 g^{-1}$
  MoVTeNbNiOx (II) = 7.33 $m^2 g^{-1}$
  MoVTeNbCrOx (I) = 11.48 $m^2 g^{-1}$
  MoVTeNbCrOx (II) = 9.42 $m^2 g^{-1}$
  MoVTeNbCoOx (I) = 5.29 $m^2 g^{-1}$
  MoVTeNbCoOx (II) = 10.56 $m^2 g^{-1}$

- Percentage of oxygen removed (%) =

$$\frac{\text{Total amount of oxygen removed (mol } g^{-1})}{\text{Total amount of oxygen of } Mo_1V_{0.3}Te_{0.23}Nb_{0.12}O_x \text{ (mol } g^{-1})} \times 100\%$$